Mon. Not. R. Astron. Soc. **000**, 1–23 (2013) Printed 9 August 2013 (MN LATEX style file v2.2)

The structure and fate of white dwarf merger remnants

Marius Dan[1,2⋆], Stephan Rosswog[2,3], Marcus Brüggen[1], Philipp Podsiadlowski[4]
[1] *Hamburger Sternwarte, Universität Hamburg, Gojenbergsweg 112, 21029 Hamburg, Germany*
[2] *School of Engineering and Science, Jacobs University Bremen, Campus Ring 1, 28759 Bremen, Germany*
[3] *The Oskar Klein Centre, Department of Astronomy, AlbaNova, Stockholm University, SE-106 91 Stockholm, Sweden*
[4] *Department of Astronomy, Oxford University, Oxford OX1 3RH, UK*

Accepted ?. Received ?; in original form ?

ABSTRACT
We present a large parameter study where we investigate the structure of white dwarf (WD) merger remnants after the dynamical phase. A wide range of WD masses and compositions are explored and we also probe the effect of different initial conditions. We investigated the degree of mixing between the WDs, the conditions for detonations as well as the amount of gas ejected. We find that systems with lower mass ratios have more total angular momentum and as a result more mass is flung out in a tidal tail. Nuclear burning can affect the amount of mass ejected. Many WD binaries that contain a helium-rich WD achieve the conditions to trigger a detonation. In contrast, for carbon-oxygen transferring systems only the most massive mergers with a total mass $M \gtrsim 2.1 M_{\odot}$ detonate. Even systems with lower mass may detonate long after the merger if the remnant remains above the Chandrasekhar mass and carbon is ignited at the centre. Finally, our findings are discussed in the context of several possible observed astrophysical events and stellar systems, such as hot subdwarfs, R Coronae Borealis stars, single massive white dwarfs, supernovae of type Ia and other transient events. A large database containing 225 white dwarf merger remnants is made available via a dedicated web page.

Key words: white dwarfs – accretion, accretion disks – nuclear reactions, nucleosynthesis, abundances – hydrodynamics

1 INTRODUCTION

White dwarfs are the most common outcomes of stellar evolution. It is estimated that there are about 10^{10} WDs in our Galaxy (Napiwotzki 2009) out of which 2.5×10^8 reside in binaries consisting of two white dwarfs (Nelemans et al. 2001). About half of these are close enough (typical orbital periods $\lesssim 8$ hr) that gravitational wave emission can drive them to a phase of mass transfer within a Hubble time. In recent years, surveys such as the ESO SN Ia Progenitor Survey (SPY) and Sloan Digital Sky Survey (SDSS) have drastically increased the number of known detached and interacting WD binaries (e.g. Napiwotzki et al. 2004; Nelemans 2005; Kilic et al. 2011). Among the about 50 known WD binaries, there are four eclipsing WD systems that allow for a very precise measurement of the masses and radii of both components (Steinfadt et al. 2010; Parsons et al. 2011; Brown et al. 2011; Vennes et al. 2011). The gravitational waves (GWs) produced by some of these systems will be within the detection limit and used as verification sources for the future space-based gravitational wave facilities, such as eLISA/NGO (Nelemans 2009; Marsh 2011; Amaro-Seoane et al. 2012).

Mass transfer critically affects the further evolution of the binary. Depending on whether it is stable or not, the WD binary may either survive the initial mass-transfer phase to become a semi-detached system or else end up merging completely. The stability of mass transfer depends sensitively on (i) the response of the two WDs to the mass transfer, (ii) on the stars' masses and (iii) on various angular momentum transport mechanisms (e.g. Marsh et al. 2004; Gokhale et al. 2007).

Once the WDs have merged, the subsequent evolution may lead to a flurry of different outcomes including He-rich hot subdwarfs of spectral type B (sdB; Saio & Jeffery 2000; Han et al. 2002; Heber 2009) and O (sdO), R Coronae Borealis (RCB) stars (Webbink 1984; Iben et al. 1996; Justham et al. 2011; Jeffery et al. 2011; Clayton 2012),

⋆ E-mail: marius.dan@hs.uni-hamburg.de

massive carbon/oxygen (CO) or oxygen/neon (ONe) WDs (Bergeron et al. 1991; Segretain et al. 1997), explosions as supernova Type Ia (SN Ia; Webbink 1984; Iben & Tutukov 1984), an accretion-induced collapse (AIC) to a neutron star (NS) (Saio & Nomoto 1985; Nomoto & Kondo 1991; Saio & Nomoto 2004) or perhaps even to a black hole (BH). For a chart that summarises the possible outcomes of WD mergers see Figure 1.

Type Ia SN find ample use as cosmological distance indicators, but, despite the existence of well-established correlations, the identity of the companion that donates the mass and the exact nature of the explosion mechanism have remained unclear. The idea that WD mergers near the Chandrasekhar mass could cause SNe Ia has been formulated decades ago (Iben & Tutukov 1984; Webbink 1984) and particularly massive cases would be natural candidates to explain particularly bright events (for example SNLS-03D3bb is more than twice as bright as a normal SN Ia; see Howell et al. 2006). More recently, it has been realized that also WD-WD systems with a total mass below the Chandrasekhar mass could be responsible for (at least a fraction) of SN Ia (Rosswog et al. 2009a; Sim et al. 2010; van Kerkwijk et al. 2010; Woosley & Kasen 2011).

A He, or hybrid He-CO, plus a CO WD could possibly lead to a thermonuclear runaway and hence a nova or a SN explosion prior or at the merger time (Guillochon et al. 2010; Dan et al. 2012). Guillochon et al. (2010) found that Kelvin-Helmholtz instabilities are able to trigger He explosions at the surface of the accretor if mass transfer is highly unstable (i.e. large $\dot{M}$) and occurs in the direct impact regime. A second detonation could be triggered by shock compression in the CO core leading to spectra and light-curves similar to "normal" SNe Ia (e.g. Sim et al. 2010). If the core fails to detonate, these events may resemble sub-luminous SNe Ia/Ib (Shen et al. 2010; Waldman et al. 2011). Alternatively, if the explosion during mass transfer is avoided, they could undergo hydrodynamical burning when the donor is tidally disrupted and plunges onto the more massive WD.

In order to understand the wealth of possible outcomes of WD–WD mergers, an exhaustive parameter study is required. Here we study these properties minutes after the merger of 225 WD-WD systems covering a large range of WD masses and chemical compositions. Our study is complementary to the work of Guerrero et al. (2004); Lorén-Aguilar et al. (2009); Raskin et al. (2011); Zhu et al. (2013). These studies investigated a smaller parameter space, used different initial conditions (with the exception of Raskin et al. 2011) and Zhu et al. (2013) did not included the feedback from nuclear burning.

We investigate whether minutes after the WD merger the conditions for hydrodynamical burning (i.e. characteristic time for heating by nuclear reactions becomes faster than the dynamic response time) that could trigger a supernova or supernova-like explosion are reached. This is complementary to the study of Guillochon et al. (2010); Dan et al. (2011, 2012) where we investigated whether hydrodynamical burning occurs during mass transfer or, later, during the final coalescence.

We provide a large database containing the thermodynamic and rotational profiles via the web page `www.hs.uni-hamburg.de/DE/Ins/Per/Dan/wdwd_remnants`, so that they can be used for subsequent stellar evolution studies.

This paper is organized as follows: in Section 2 we briefly describe our numerical methods and in Section 3 we present our results in detail. Specifically, §3.1 is devoted to the structure of the merger remnants, § 3.2 to a comparison between the results obtained with corotating and non-rotating initial conditions, § 3.3 to an analysis of mixing between the binary components, § 3.4 to whether conditions for hydrodynamical burning occur, § 3.5 to a discussion of how the unbound mass and angular momentum depend on the stars' masses, § 3.6 to a resolution dependence study and § 3.7 to a detailed comparison to previous work. In Section 4 we discuss the applications of our simulations to astrophysical systems. In Section 5 we summarize our results.

2 NUMERICAL METHODS AND INITIAL CONDITIONS

Our numerical code and initial conditions have been described in detail in the literature (Rosswog et al. 2004, 2008; Dan et al. 2011, 2012), therefore we only briefly summarize the main ingredients of the adopted approach. We use a 3D smoothed particle hydrodynamics (SPH; for recent reviews see Monaghan 2005; Rosswog 2009) code that treats shocks by means of an artificial viscosity scheme with time dependent parameters (Morris & Monaghan 1997; Rosswog et al. 2000) so that viscosity is essentially absent unless it is triggered. Moreover, a switch is applied to suppress the viscous forces in pure shear flows (Balsara 1995). We use the binary tree of Benz et al. (1990) to search the SPH neighbors and to calculate the gravitational forces. The code uses the Helmholtz equation of state (Timmes & Swesty 2000) which is coupled to the minimal nuclear reaction network of Hix et al. (1998) to include the energetic feedback onto the gas and to obtain (approximate) information on the nuclear composition.

To construct the initial stars the SPH particles are placed on a stretched hexagonal lattice (Rosswog et al. 2009b) and provided with the properties derived from solving the Lane-Emden equations. The particle distribution is subsequently relaxed in isolation at $T = 10^5$ K and a velocity-dependent force is applied to drive them to equilibrium. As before (Dan et al. 2012), we use exemplary chemical compositions, in nature also alternative compositions may be realized that depend on the exact evolutionary history of the stars. Below 0.45 $M_\odot$ our WDs are made of pure helium, between 0.45 and 0.6 $M_\odot$ they have a 0.1 $M_\odot$ helium mantle and a pure carbon-oxygen core (mass fractions $\mathrm{X}(^{12}\mathrm{C}) = 0.5$ and $\mathrm{X}(^{16}\mathrm{O}) = 0.5$); between 0.6 and 1.05 $M_\odot$ WDs are made entirely of carbon-oxygen with mass fractions $\mathrm{X}(^{12}\mathrm{C}) = 0.4$ and $\mathrm{X}(^{16}\mathrm{O}) = 0.6$ uniformly distributed through the star and above 1.05 $M_\odot$ they are made of oxygen, neon and magnesium with $X(^{16}\mathrm{O}) = 0.60$, $X(^{20}\mathrm{Ne}) = 0.35$ and $X(^{24}\mathrm{Mg}) = 0.05$, respectively.

It is not well known what the WD spins are at the

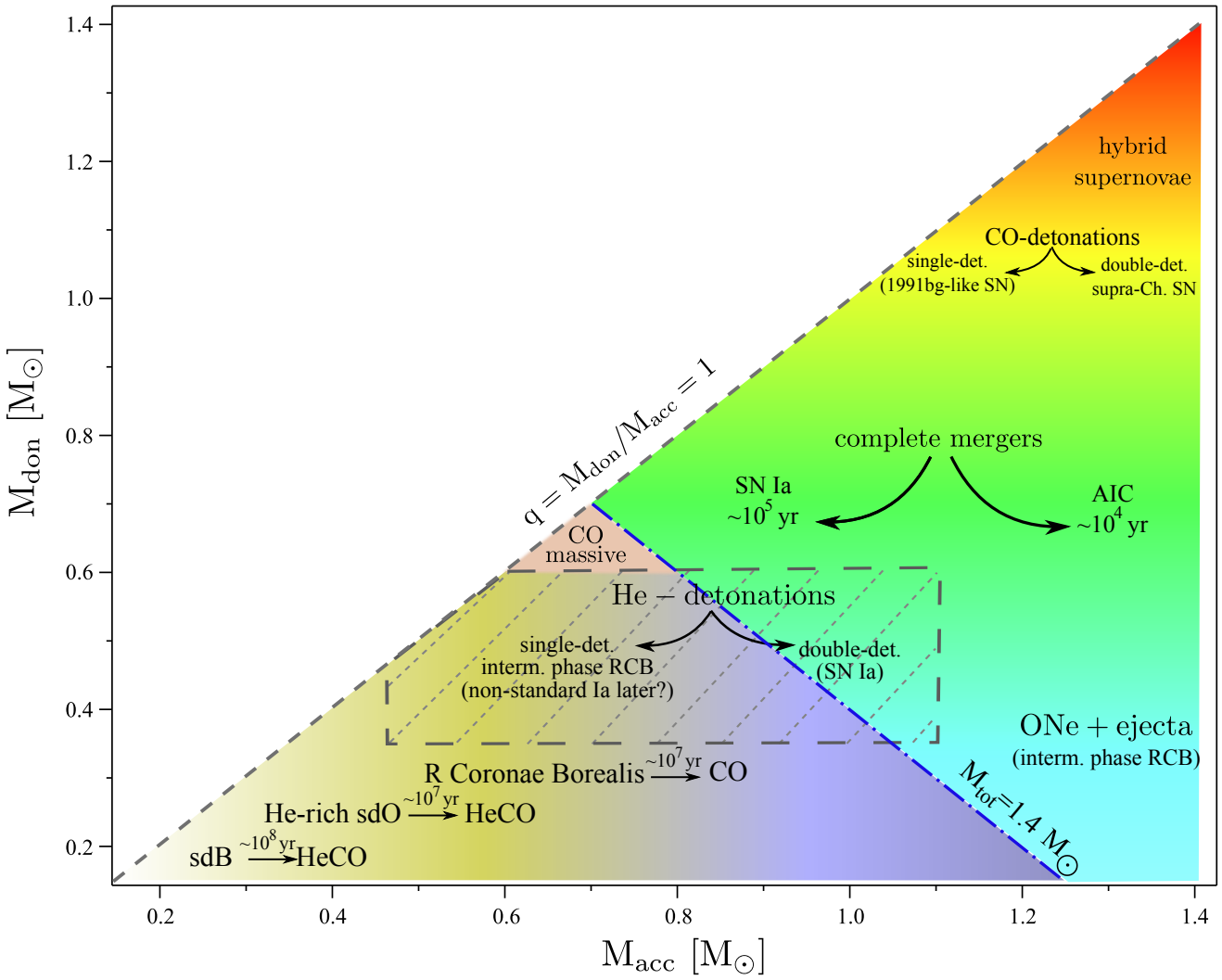

Figure 1. Binary evolution predicts that a good fraction of the total number of double white dwarf systems will come into contact within a Hubble time and, via merging, they could lead to a variety of outcomes, depending mainly on the masses of the donor and the accretor, $M_{\rm don}$ and $M_{\rm acc}$, respectively. The potential WD merger products are helium-rich subdwarfs (sdB and sdO stars), R Coronae Borealis stars, high-mass CO/ONe white dwarfs, neutron stars, Type Ia supernovae and low-mass black holes, see text for additional details. The hashed region roughly marks the region where we found helium-detonations during the mass transfer and at the merger moment (see Dan et al. 2011, 2012). As we will show in Section 3, minutes after the merger a good fraction of these systems can still undergo dynamical burning.

moment when numerically resolved mass transfer sets in (our initial mass transfer rates are well above the Eddington limit). The work of Fuller & Lai (2012); Burkart et al. (2012) suggests that a coupling between tides and stellar pulsations may drive the binary to a corotating state prior to mass transfer initiation. Since it is physically plausible and computationally convenient, we start our simulations from corotating initial conditions. The technical procedure how to construct an equilibrium fluid configuration has been explained in detail before (Rosswog et al. 2004; Dan et al. 2011) and we refer the interested reader to this work and the references cited therein. In Dan et al. (2011) we had demonstrated the sensitivity of the orbital and mass transfer evolution on the initial conditions. In particular we found that approximate initial conditions can underestimate the duration of the phase of (numerically resolvable) mass transfer by orders of magnitude and that they, containing the wrong amount of angular momentum, also impact on the resulting remnant structure. Generally, approximate initial conditions lead to a too fast inspiral and to too large densities and temperatures. How serious this is for the further evolution depends on the system under consideration.

We scan the parameter space with as many as 225 simulations which are summarized in Table A1 in the appendix. The masses of the donor stars range from 0.2 to 1.05 $M_\odot$, those of the accretors from 0.2 to 1.2 $M_\odot$, both ranges are probed in steps of 0.05 $M_\odot$. In this broad parameter scan, each binary system is modeled with only 40 000 SPH par-

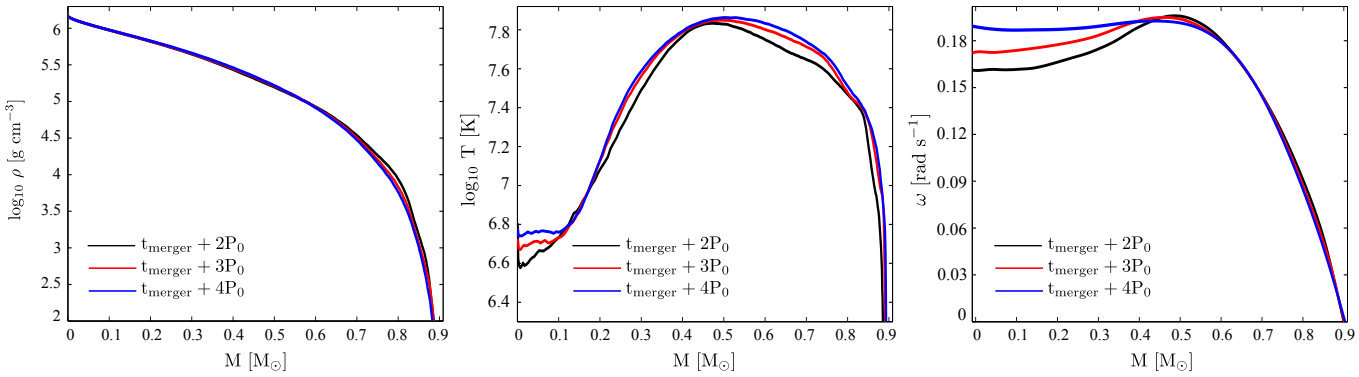

Figure 2. Remnant evolution for the $0.45 + 0.45\,M_\odot$ system between 2 (red line), 3 (blue line) and 4 (black line) times the initial period since the merger moment, $t_{\rm merger}$. Shown are density (left), temperature (center) and angular velocity (right) profiles, averaged over equipotential surfaces, as a function of enclosed mass from the center of the accretor. The evolution of the remnant at this stage is driven by the artificial viscosity. The core is spun up and evolves towards rigid rotation, the temperature increases overall and the density is increasing in the core and decreasing in the outer regions. Overall the properties do not change much and as the remnant evolves there is even less variation in its properties.

ticles. While this does certainly not yield fully converged results, our analysis in §3.6 suggests that the qualitative results and trends are robust. This study is intended to identify interesting systems, they should be studied in more detail at higher resolution in the future.

3 RESULTS

First results from the WD systems that we study have been presented in Dan et al. (2012). Here we give a more complete overview over the parameter space. We determine the remnant properties at a time of three initial orbital periods after the moment when the donor is fully disrupted and its center of mass cannot be identified anymore. At this point we stop the calculations since the dynamical evolution is essentially over and the changes occur at a much more moderate pace. We illustrate this in Figure 2 for a system of two 0.45 $M_\odot$ WDs. Density, temperature and angular velocity are averaged over equipotential surfaces and are shown as a function of the enclosed mass at two, three and four initial orbital periods after the merger moment. The density profile hardly changes during this time span, but numerical dissipation damps out the differential rotation in the core which goes along with a secular increase in the temperature. We repeated this analysis for systems of $0.2 + 0.8\,M_\odot$, $0.45 + 1.0\,M_\odot$ and $0.8 + 0.9\,M_\odot$ and found very similar results.

3.1 Remnant profiles

Figure 3 gives an overview over the morphology for the whole range of mass distributions at the moment when the simulations are stopped ($t_{\rm merger} + 3P_0$). This is different from Figure 7 in Dan et al. (2012) where the configuration was shown at the moment when the conditions are most promising for explosion. At the merger point about 1% of the system's total mass is flung out into a tidal tail. Most of this material is still gravitationally bound to the central remnant and it will fall back, interact with and shape the outer disk. Systems with a mass ratio close to unity (those near the diagonal dashed line) lead to an almost spherical remnant with little material in the tidal tail, while smaller mass ratio systems (lower right corner of the digram) have a more extended tail.

Based on temperature, density and rotation profiles, we can distinguish different regions in the remnant as shown in Figure 4 for a $0.6 + 0.7\,M_\odot$ binary system. We identify four main regions of the remnant: a cold (nearly) isothermal core; a hot envelope; a centrifugally supported Keplerian disk and a tidal tail. Fits for the masses of these regions can be found in the Appendix (Eqs. A5 - A8).

The degree of heating experienced by the core is closely related to the degree of mixing of the two stars (discussed in more detail in Sec. 3.3) and increases with the mass ratio. For a mass ratio of $q \sim 0.7$ the mass of the core and the disk plus envelope are equal, with the mass of the core decreasing down to 30% of the total mass for a mass ratio of unity, see left panel of Figure 5. In our simulations, even equal mass cases do not lead to perfectly symmetric remnants. This is because the systems reacts sensitively to even small deviations from perfect symmetry. At some point during the dozens of orbits of inspiral and mass transfer (Dan et al. 2012) a small numerical imperfection can kick-start the (asymmetric) disruption process. Consequently, the two spiral arms that form right after the merger have different sizes, with the smaller one quickly dissipating. Thus the core of the remnant is always a fraction of the star that is not fully disrupted and it is colder than the surrounding region, see Figure 6. A perfectly symmetric system, however, is a completely academic case and therefore such systems should be considered as only nearly perfectly symmetric.
Recent studies of Lorén-Aguilar et al. (2009); Pakmor et al. (2010, 2011); Zhu et al. (2013) found that both components are symmetrically disrupted and the higher temperature is located at the remnant's center. We were able to reproduce their results, but only when we started with their approxi-

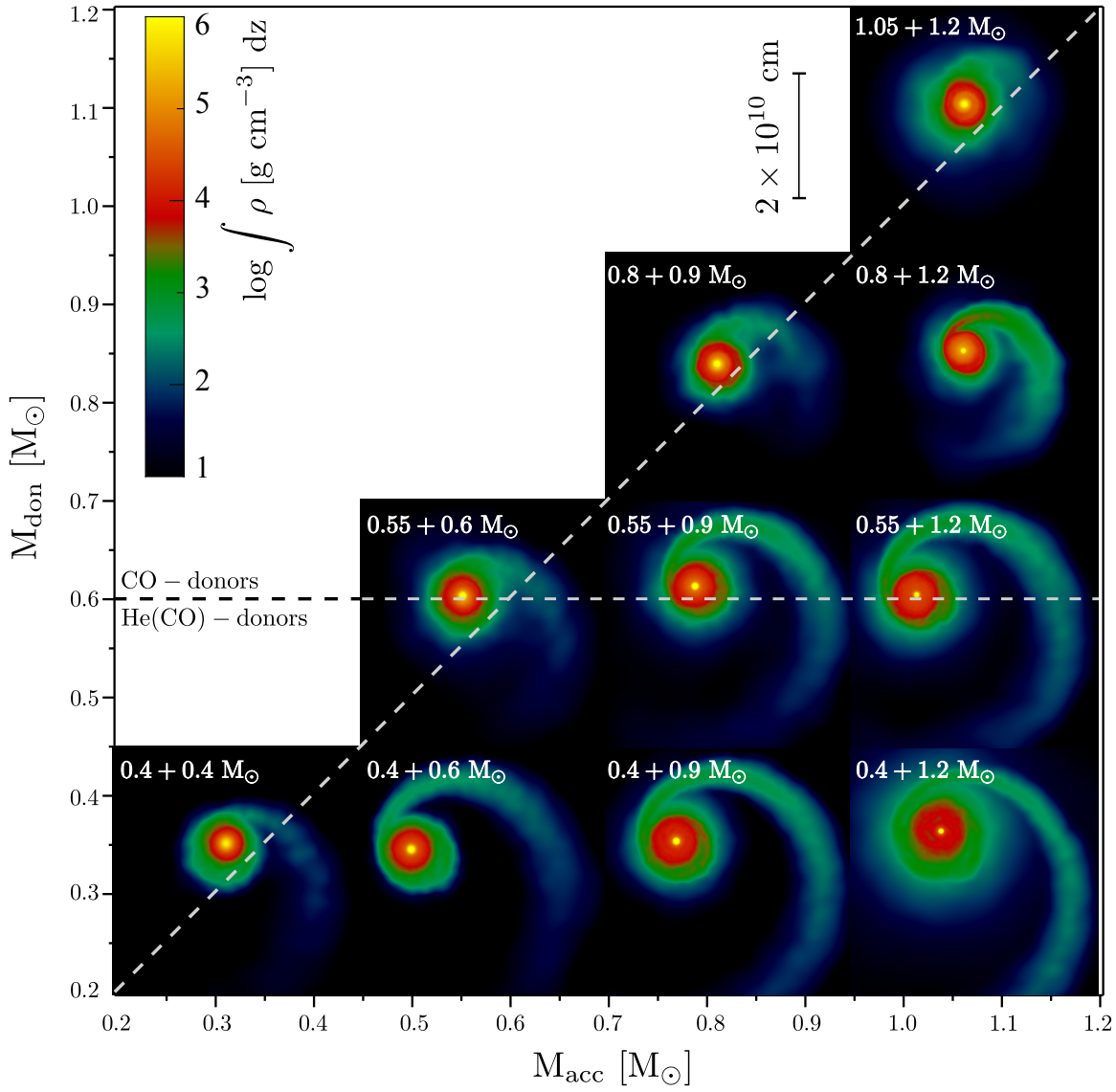

Figure 3. Column density snapshots taken after a timescale of three initial periods after the merger moment. This corresponds to the moment at which we analyze all merger remnants presented in Table A1 in the Appendix. The 10 snapshots shown here are representative of all white dwarf chemical composition and mass combinations. The horizontal dashed line divides the CO- and He-mass-transferring systems and the diagonal dashed line shows where the masses of the binary's components are equal, ie. the mass ratio $q = M_{\rm don}/M_{\rm acc} = 1$. During the merger, because the matter coming from the former donor has a high angular momentum and cannot be accreted directly by the accretor, a disk and a tidal tail will form. For the systems with a lower mass ratio q the matter has a larger specific angular momentum causing the disk to spread over a larger distance and a more extended tail.

mate initial conditions, neglecting the tidal deformation of the two stars, see Section 2.

The right panel of Figure 5 shows the enclosed mass as a function of the radius from the center of the accretor with $1.2\,M_\odot$ and donor masses ranging from 0.3 to 1.0 $M_\odot$ three initial orbital periods after the merger. The solid black line shows the result from the beginning of mass transfer, at $t = 0$ s. Comparing the central density of the remnant with that at the moment when mass transfer sets in, we find that it changes by as much as 30%. For low mass ratios the core experiences an expansion as the accretor is heated through shocks while for higher mass ratios the core is compressed by the massive outer material.

The hottest region of the remnant is the region between the central core and the surrounding disk. In this region matter is nearly virialized. Up to about 0.1 $M_\odot$ (decreasing with increasing mass ratio q) has been accreted prior to the actual merger (Dan et al. 2011). We distinguish between the disk

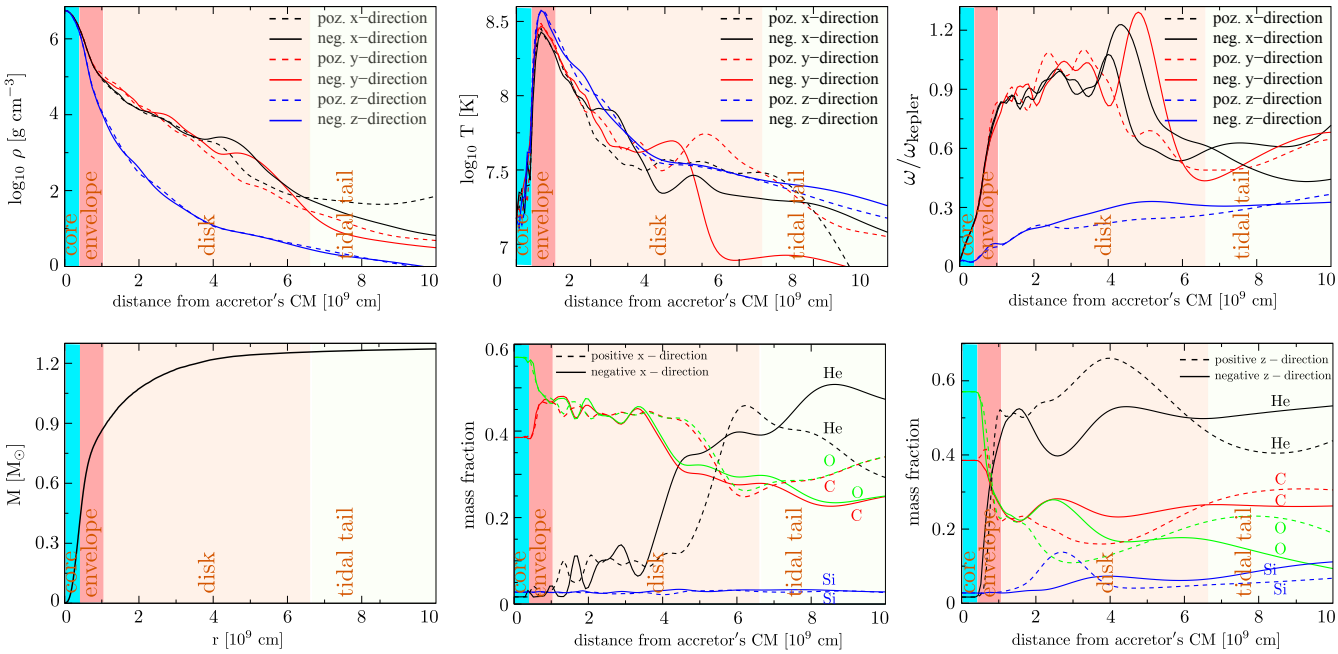

Figure 4. The different regions of the remnant are shown here in the density (top left), temperature (top center), angular velocity (top right), enclosed mass (bottom left) and mass fractions along X- (bottom center) and Z-axes (bottom right) profiles for the system with $0.6 + 0.7\ M_\odot$. Here the quantities are SPH-interpolated values along different positive and negative directions with respect to the former accretor's center of mass. We distinguish between the different regions based on the temperature, density and angular velocity profiles. The central region of the former accretor is nearly isothermal and forms the core (cyan region). The outer edge of the core is taken where there is a steep increase in temperature. Its outer regions have been heated up during the mass transfer and at the merger moment and together with a fraction of the matter coming from the donor it forms the hot, thermally supported envelope (light red region). The hot envelope is surrounded by a (nearly) Keplerian disk (light orange region) and a fraction of the total mass is flung out in a tidal tail (light yellow region) that will fallback and reshape the outer region of the disk.

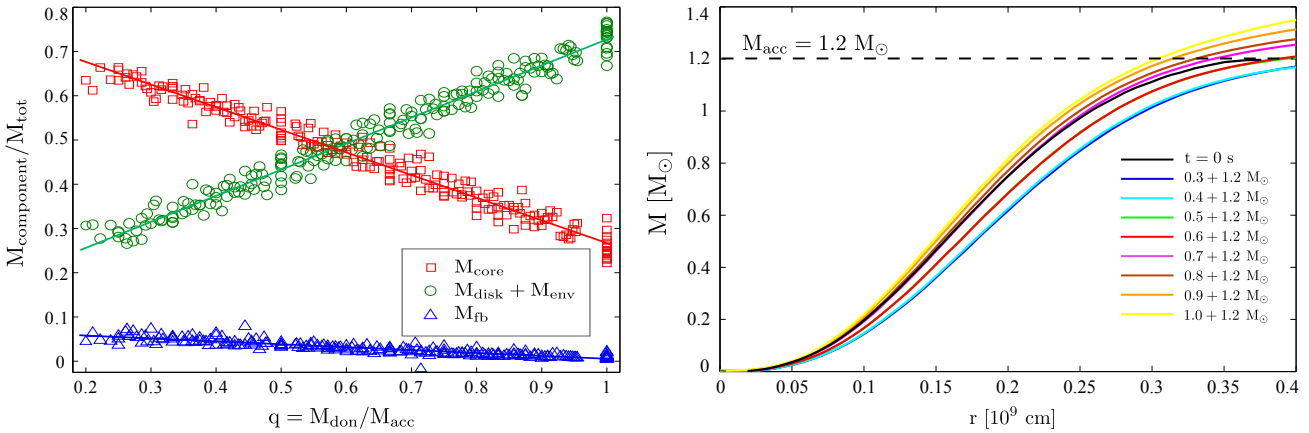

Figure 5. (left) Mass of the core (red squares), hot envelope plus disk (green circles) and tidal tail material (blue triangles) as a function of mass ratio $q = M_{\rm don}/M_{\rm acc}$. The degree of heating experienced by the core is increasing with the mass ratio. The mass of the core and the envelope plus disk are equal at around $q = 0.7$ with the mass of the core decreasing down to 30% of the total mass for a mass ratio of unity. The mass of the fallback material $M_{\rm fb}$ increases with decreasing mass ratio. Continuous lines are fits to the data, see Eq. A5-A8 in the Appendix. (right) Enclosed mass as a function of radius with respect to the WD center of mass for the remnants with $1.2\,M_\odot$ accretor and donor masses ranging from 0.3 to 1.0 $M_\odot$. For low mass ratios the core experiences an expansion as the accretor is heated through shocks while for higher mass ratios the core is compressed by the massive outer material.

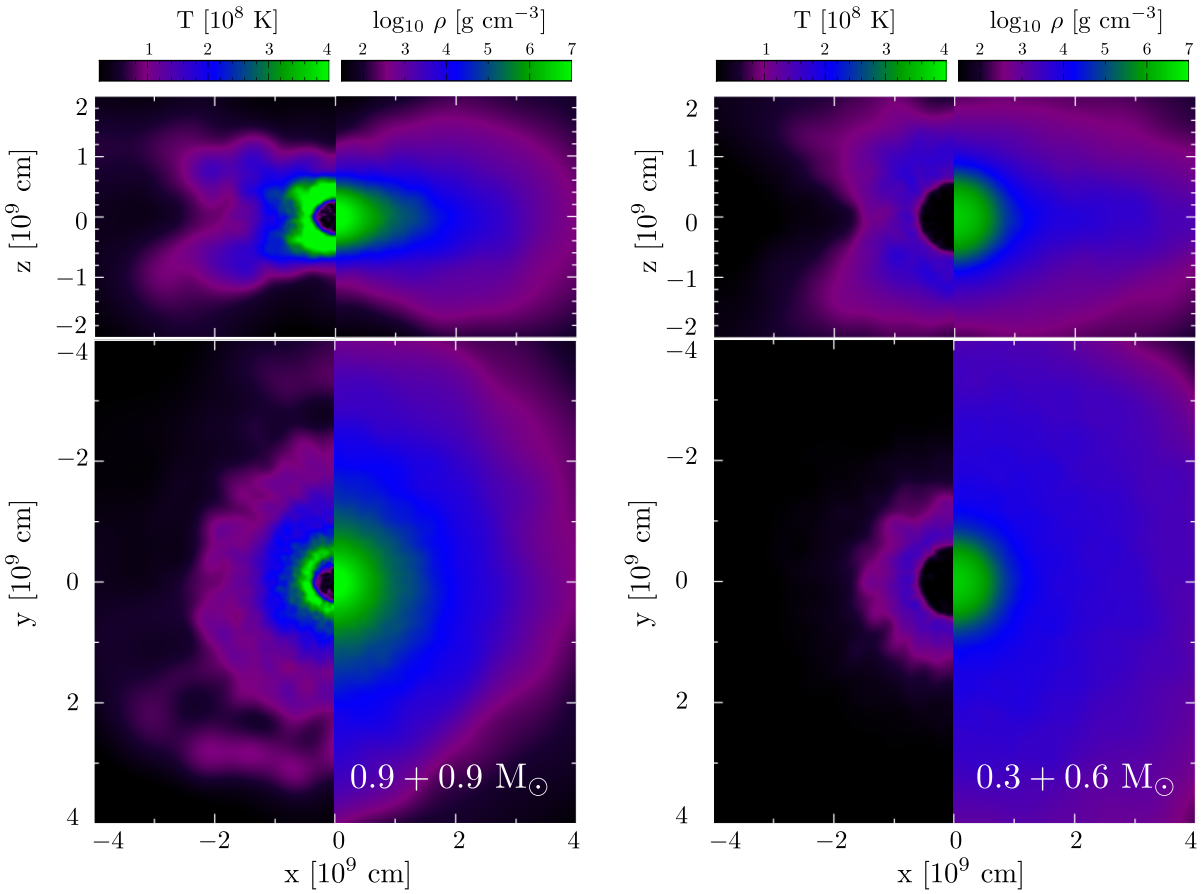

Figure 6. Comparison of the final remnants resulting from the mergers of $0.9+0.9\,M_{\odot}$ (left) and $0.3+0.6\,M_{\odot}$ (right) in both XZ (upper panels) and XY (lower panels) planes. Within each panel, the left subpanel shows the temperature and the right panel the density. The degree of heating experienced by the core increases with the mass ratio. However, the central region (core) is always colder than the surrounding region (envelope), even for systems with a mass ratio q of unity.

and the hot envelope based on the angular velocity profile, as shown in the top-right of Figure 4. The peak temperature is located in the envelope, corresponding fit formulae can be found in the appendix (Eqs. A1 and A2).

While the envelope is supported against gravitational attraction mainly by the thermal pressure, the disk is centrifugally supported and much of its material has not been shocked. The disk plus envelope extent increases with the mass ratio for a constant total mass. Additionally, there is a clear tendency to increase the disk plus envelope extent with the total mass for a fixed mass ratio.

The disk is fed by the matter in the trailing arm which is still bound to the central remnant. The fallback material has a spiral shape and does not rotate at a Keplerian speed. The amount of matter flung out increases with decreasing mass ratio, see Figure 5, and with increasing total mass of the system. Assuming this material is ballistically falling towards the central remnant we calculate how much it takes for the matter to circularize (as described in Rosswog 2007). We find that the fallback time for runs simulated here is ranging from days to years and most of the material will circularize inside the initial radius of the disk. For example for the system with $0.6+0.9\,M_{\odot}$ only 3% of the material falling back will circularize beyond the disk.

Fryer et al. (2010) computed light-curves for explosions of Chandrasekhar mass WDs surrounded by a debris of material, left after the merger of two massive WDs. They used the merger of a $0.9+1.2\,M_{\odot}$ system to constrain the density profiles of the material surrounding the central remnant and found that the density follows an r^{-4} profile. To account for possible variations in the density profile they also did one calculation assuming a shallower $\propto r^{-3}$ profile. In Figure 7 we show the density profiles of the remnant's outer regions for different systems. They all share the same accretor mass of $1.2\,M_{\odot}$ but have different donor masses of 0.3, 0.4, 0.6 (upper panels), 0.7, 0.8 and 0.9 $M_{\odot}$ (bottom panels). We use two different colors to identify the particles formerly belonging to the accretor (blue triangles) and the donor (black dots). The red dashed-line shows the fitted density profile, as steep as $r^{-3.8}$ for the highest mass ratio binary, while the lowest mass ratio one has a $r^{-3.5}$. We observe the same trend over the entire WD-WD parameter space, the profile becomes shallower (ie. value of exponent increases) with decreasing mass ratio and the donor's density, ranging from

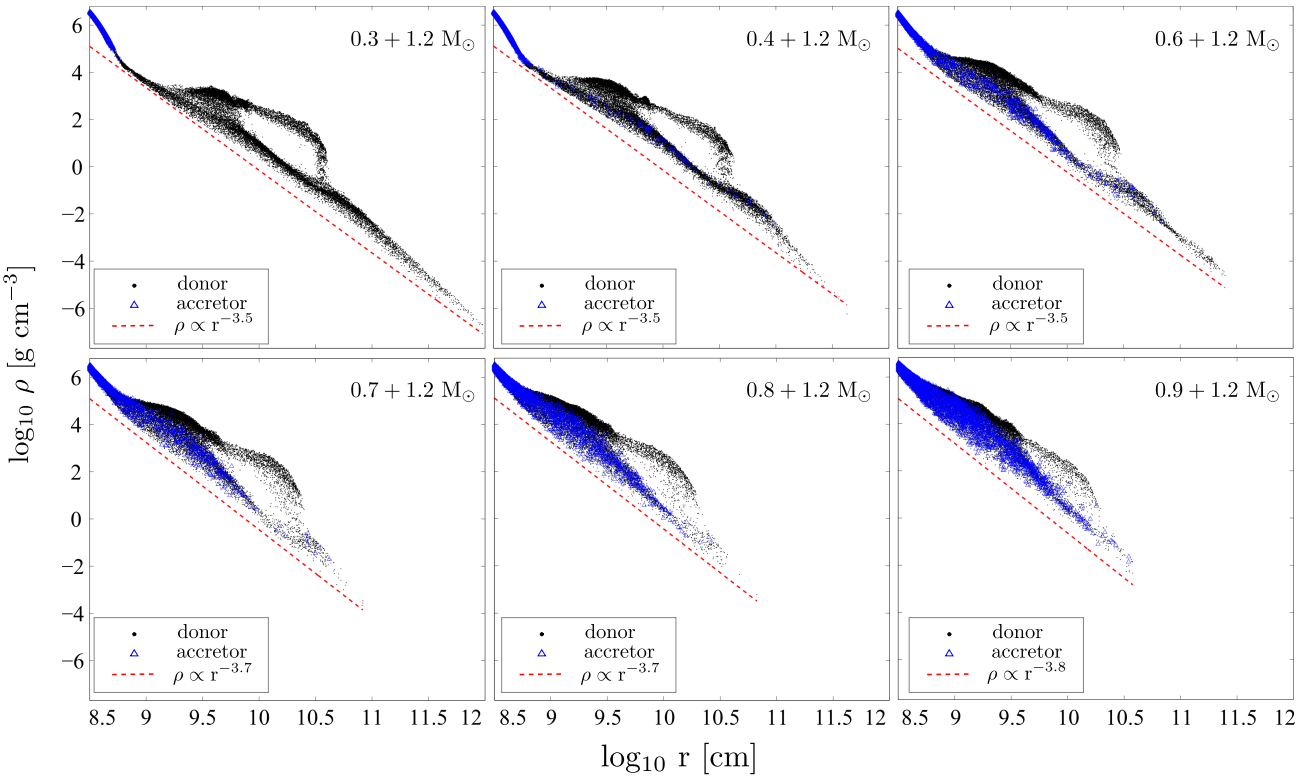

Figure 7. Density profiles of the outer region of the remnant as a function of the radius with respect to the former accretor's center of mass for the systems with an accretor of 1.2 $M_\odot$ and donor masses between 0.3 and 0.9 $M_\odot$. The blue triangles and black dots are the particles that belong to the former accretor and donor, respectively. The dashed red line is the linear fitted density profile and it ranges from a $r^{-3.8}$ to $r^{-3.5}$.

$r^{-3.9}$ to $r^{-3.3}$. As discussed by Fryer et al. (2010), in a supernova explosion, a shallower density profile will cause the radiation to be trapped for a longer time and the shock breakout will have a lower, later X-ray luminosity peak and longer duration.

In the Appendix we provide fit formulae for the maximum angular velocity, $\omega_{\rm max}$, and the mass inclosed inside of it.

3.2 Spin dependence

Since the initial rotational state of a white dwarf binary is not well known and this study is investigating the initially tidally locked systems, it is interesting to ask to which extent the results would change for a different initial spin state. This is of particular relevance with respect to the question where in the remnant a possible thermonuclear ignition could be triggered.

The major difference between a tidally locked and a non-rotating binary comes from the fact that in the latter case the stars appear in the binary frame to rotate against the orbital direction and therefore at contact produce a shear layer with a velocity discontinuity of $\Delta v \sim 2R_*\omega_{\rm orb}$. In the perfectly co-rotating case, in contrast, the velocities vanish in the binary frame, in reality small velocities occur due to the stars dynamically adapting to the changing gravitational field of the companion. As a consequence, non-rotating stars with their substantially larger shear produce a more pronounced string of Kelvin-Helmholtz vortices that can subsequently merge. This behaviour has been explored in detail in the context of neutron star mergers, see e.g. Ruffert et al. (1996); Rosswog et al. (1999); Rasio & Shapiro (1999); Rosswog & Davies (2002); Price & Rosswog (2006); Rosswog et al. (2013); Zrake & MacFadyen (2013), but it occurs in a qualitatively similar way also for WD binaries.

To explore the spin dependence we set up a binary system with twice 0.89 $M_\odot$ and 2×10^5 particles exactly like in Pakmor et al. (2010) and another such system with the same particle number, but in a tidally locked state prepared as described in Dan et al. (2011). The non-spinning system merges quickly and does not have much time to develop large asymmetries (this may be partially aided by the approximate initial conditions that we apply here for comparison reasons). We find that in carefully relaxed co-rotating systems the merger occurs on a much longer time scale and the final merger is initiated once a small numerical perturbation breaks the perfect initial symmetry. In Figure 8 we compare the two systems at the moments when they are most prone to detonation ($t = 130$ s for the non-rotating, left panels, and at $t = 719$ s for the tidally locked case, right panels). Apart from the different morphology one sees the result of the much stronger Kelvin-Helmholtz instabilities for the non-rotating case: pronounced hot vortices form in the high-density core

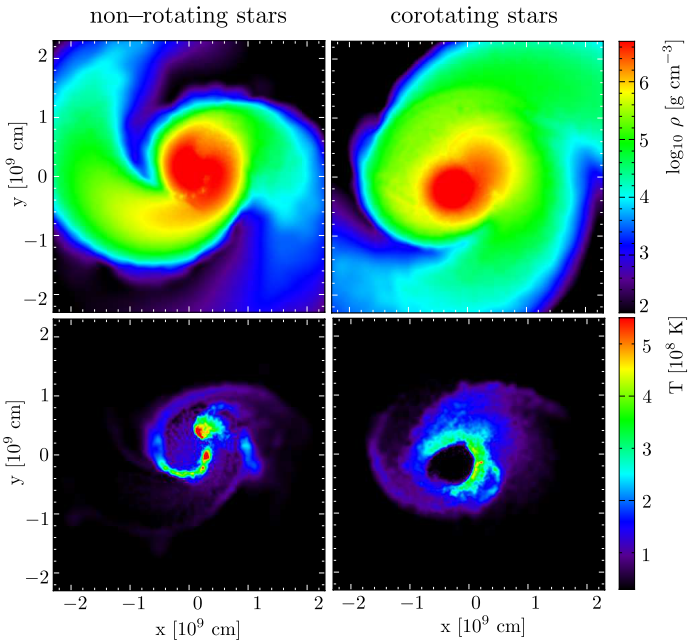

Figure 8. Comparison of the outcome of different spin states. Each time a binary with 0.89 $M_\odot$ is prepared, once with non-rotating (left column) and once with tidally locked stars (right column). Both cases are shown at the moment when they are most prone to detonation (t = 130 s, left, and t = 719 s, right column.

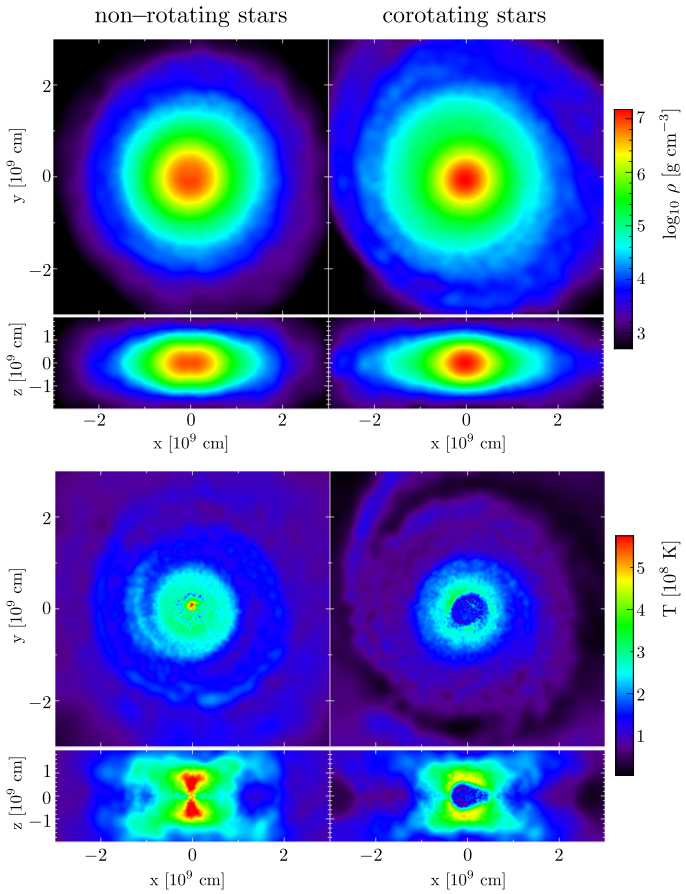

Figure 9. Dependence of the remnant structure on the initial white dwarf spin. The left column shows the results for the initially non-rotating stars, the right column for an initially tidally locked binary, both stars have 0.89 $M_\odot$. The non-spinning stars merge quickly and develop the hottest temperatures in their core, while the corotating system orbits for much longer until a numerical perturbation finally breaks the symmetry. The hottest regions in this case are the surface layers of the resulting merger core.

at the interface between the stars. They are also visible as density troughs in the upper-left panel. The corotating case, in contrast, shows that the locations most prone to detonation are at lower densities and temperatures, at the surface rather than the centre of the high-density core. The final density and temperature distributions are shown in Figure 9, both for XY- and the XZ-plane. Once the Kelvin-Helmholtz vortices have merged, they result in a 'hour-glass' shaped temperature distribution. This is agreement with the findings of Zhu et al. (2013) (and with those for neutron star mergers; Rosswog et al. 2013).

This comparison illustrates that the spin state has a serious impact on the location where an explosion is likely triggered. Co-rotating systems likely ignite in the surface layers of the remnant core, while in irrotational systems explosions likely come from the central and highest density regions of the core. Therefore, corotating and irrotational systems should differ in the amount of unburnt material, their ejecta velocities and their degree of asymmetry.

3.3 Mixing of matter between the binary components

In Figure 10 we show the fraction of the mass that originally belonged to the donor star as a function of the mass enclosed by a common equipotential surface. For mass ratios below $q \approx 0.45$, the stars hardly mix at all, while for a mass ratio close to unity maximum mixing occurs. Contrary to Zhu et al. (2013), we never find a complete mixing between the two stars. This is due to the different initial spin states (no spin in their study, tidal locking in ours) and it is consistent with the above findings of the spin dependence.

In Figure 11 we investigate how the stars mix chemically. To this end we plot averages of the mass fractions of the 7 species of our nuclear network over equipotential surfaces for ten selected binary systems. For systems below ~ 1.0 $M_\odot$ burning is negligible and only mixing occurs, see for example the shown $0.4 + 0.6$ $M_\odot$ system. This is consistent with our later discussion about dynamical burning, see Figure 12, left panel. Some burning occurs in the outer layers of the $0.55 + 0.6$ $M_\odot$ system which transforms He into Si-group elements (magenta line). This matter is finally ejected. As shown below, we find several cases where nuclear energy production contributes substantially to the mass ejection process. For He transferring systems with larger mass substantial burning may occur, the $0.4 + 1.2$ $M_\odot$ system, for example, burns roughly 0.1 $M_\odot$ of He into C.

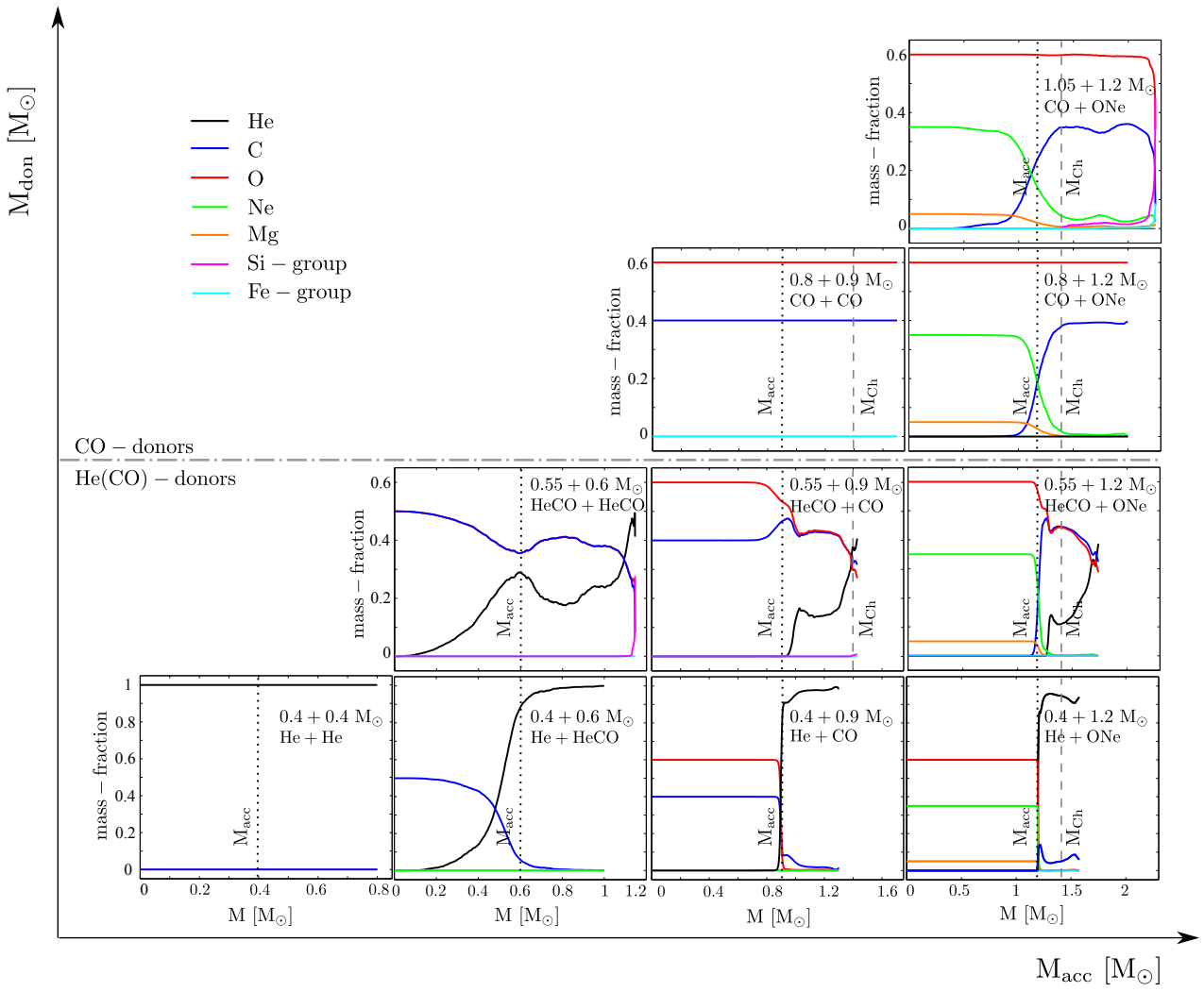

Figure 11. Mixing of the two stars during the dynamical merger phase. Shown are the mass fractions of different nuclear species for the same systems as above. The mass fractions are averages over equipotential surfaces and plotted against the enclosed mass. The horizontal dot-dashed line shows the transition from CO to He(CO) mass-transferring systems, the vertical dashed lines show the Chandrasekhar mass limit for a white dwarf and the dotted lines show the mass of the accretor.

3.4 Dynamical burning and possible detonations

Figure 12 shows the maximum temperatures at the end of the simulations and the densities at which they occur. In the left panel we show the quantities directly as extracted from the simulation, the right panel is similar, but now we use more conservatively the maximum of the SPH-interpolated values of the temperatures, $\langle T \rangle$. For an explicit discussion of this difference, we refer to Sec. 4.1 in Dan et al. (2012). The figure shows the clear trend that both the maximum temperatures $T_{\rm max}$ and the densities where they occur increase with the total system mass $M_{\rm tot}$. We have not found such a trend with respect to the mass ratio q, though. The temperatures of the matter in the hot envelope region are typically a good fraction of the virial temperature $T_{\rm vir} = GM_{\rm acc}m_{\rm p}/(3R_{\rm acc}k_{\rm B})$, where $G, m_{\rm p}$ and $k_{\rm B}$ are gravitational constant, proton mass and Boltzmann constant, respectively. Typically, we find values of $T_{\rm max} \approx 0.77T_{\rm vir}$ and $\langle T \rangle_{\rm max} \approx 0.62T_{\rm vir}$.

Dynamical burning and possibly a detonation sets in when matter heats up more rapidly than it can expand, cool and quench the burning processes, i.e. when $\tau_{\rm nuc} \leqslant \tau_{\rm dyn}$. Here, $\tau_{\rm nuc} = c_p T/\dot{\epsilon}_{\rm nuc}$ (e.g. Taam 1980; Nomoto 1982a) is the nuclear, $\tau_{\rm dyn} \approx 1/\sqrt{G\rho}$ the dynamical timescale and c_p is the specific heat at constant pressure (taken from the Helmholtz equation of state). The nuclear energy generation rate $\dot{\epsilon}_{\rm nuc}$ is calculated analytically. For CO composition we use (Blinnikov & Khokhlov 1987)

$$\dot{\epsilon}_{\rm nuc,cc} = \rho q_{\rm c} A_{T9} Y_{\rm C}^2 \exp(Q/T_{9a}^{1/3}), \qquad (1)$$

where $q_{\rm c} = 4.48 \times 10^{18}$ erg mol^{-1}, $A_{T9} = 8.54 \times 10^{26} T_{9a}^{5/6} T_9^{-3/2}$ (Fowler et al. 1975), $Y_{\rm C}$ is the ^{12}C abundance, $T_{9a} = T_9/(1 + 0.067T_9)$, $Q = 84.165$ and $T_9 = T/10^9$ K. $\tau_{\rm nuc,cc}$ is multiplied by the factor $\Theta = 3T_9/(QT_{9a}^{2/3})$ to account for the shortening of the reaction time scale due

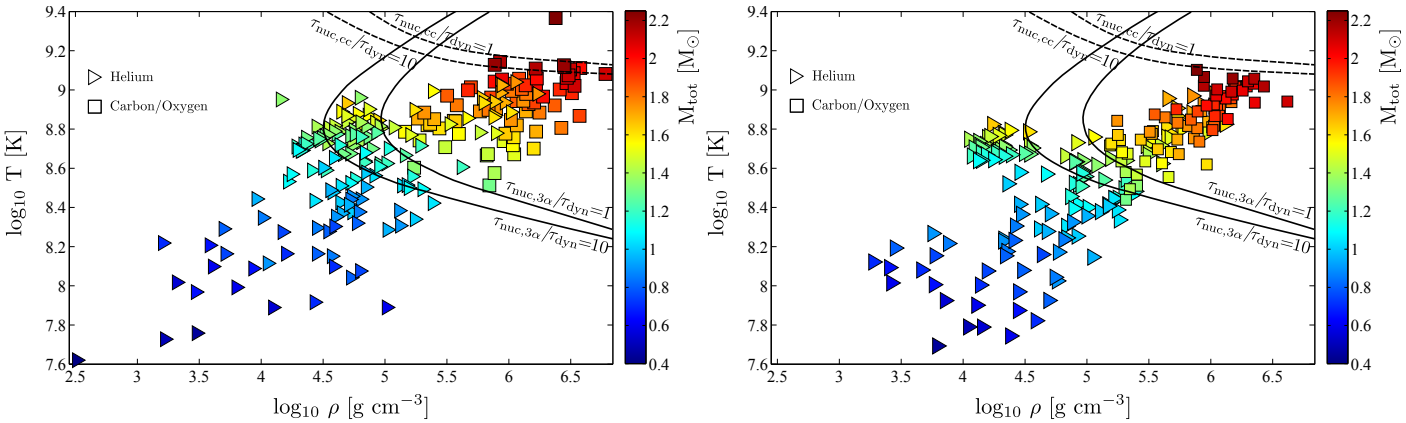

Figure 12. Left: maximum temperature $T_{\rm max}$ and density at maximum temperature $\rho(T_{\rm max})$ for both He (triangles) and CO (squares) mass-transferring systems. Right: maximum of SPH-smoothed temperatures $\langle T\rangle_{\rm max}$ and averaged density at the location of averaged maximum temperature $\rho(\langle T\rangle_{\rm max})$, again for both He (triangles) and CO (squares) mass-transferring systems. On each panel color coded is the total mass of the system, $M_{\rm tot}$. Also shown are the contours for which the timescale for triple-α reactions $\tau_{\rm nuc,3\alpha}$ and the nuclear timescale of carbon burning $\tau_{\rm nuc,cc}$ are equal or ten times larger than the dynamical timescale $\tau_{\rm dyn}$. $\tau_{\rm nuc}/\tau_{\rm dyn} \leqslant 1$ is the condition required to initiate the dynamical burning and potentially trigger a detonation.

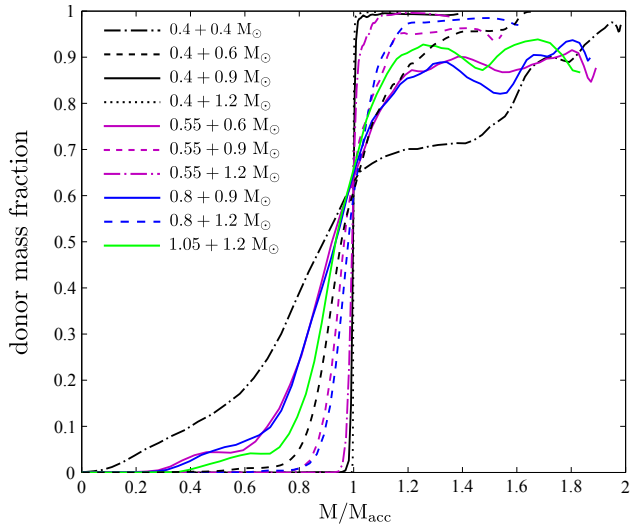

Figure 10. Mixing of the two stars during the dynamical merger phase. Shown is the donor mass fraction as a function of the mass enclosed by given equipotential surfaces (scaled to the accretor's initial mass $M_{\rm acc}$). Ten systems covering the full parameter space of mass and chemical composition (same systems as in Figure 3) are shown. The mixing between the binary components increases with the mass ratio, but it never becomes complete even for systems with a mass ratio of unity. This is due to the initially tidally locked spin state (in contrast, Zhu et al. (2013) find for their non-spinning white dwarfs complete mixing for a mass ratio $q = 1$).

to self-acceleration of burning (Frank-Kamenetskii 1967). The energy generation rate due to the triple-alpha reaction is (e.g. Kippenhahn & Weigert 1990)

$$\dot{\epsilon}_{\rm nuc,3\alpha} = 5.09 \times 10^{11} f_{3\alpha} \rho^2 X_4^3 T_8^{-3} \exp(-44.027/T_8), \quad (2)$$

where $f_{3\alpha} = \exp(2.76 \times 10^{-3} \rho^{1/2} T_8^{-3/2})$ is the weak electron screening factor (Salpeter 1954; Clayton 1968), X_4 is the mass fraction of ^{4}He (we assume pure He) and $T_8 = T/10^8$ K.

Focussing on the more optimistic estimates in the left panel of Figure 12, we see that all He accreting systems with a total mass beyond 1.1 $M_\odot$ undergo He detonations. These are roughly the same systems that are expected to produce surface detonations either from instabilities within the accretion stream and/or at the moment first dynamical contact (Guillochon et al. 2010; Dan et al. 2012). For He mass-transferring systems, neutrino cooling does not become important in comparison to burning unless temperatures in excess of 5×10^9 K are reached (see Figure 2 in Rosswog et al. 2008).

For the CO systems, above a temperature of about 6×10^8 K (e.g. Yoon et al. 2007) the energy released from C-burning is larger than neutrino losses, but these systems never reach the necessary criterion for dynamical burning $\tau_{\rm nuc,cc} \leqslant \tau_{\rm dyn}$. However, the conclusion may be different if the WDs carry a thin He surface layer ($\sim$ 1% by mass). Raskin et al. (2011) found He detonations at the surface of the accretor ($\sim 1.0\,M_\odot$) but those were not sufficiently energetic to trigger C ignition. First calculations of the expected electromagnetic display of a SN Ia explosion caused by CO-CO mergers have recently been calculated (Pakmor et al. 2010; Fryer et al. 2010). In both approaches the explosion had been artificially initiated at heuristically chosen locations, the resulting lightcurves and spectra did not match those of the most common SN Ia. Nevertheless, this topic warrants further exploration.

Binaries with total masses beyond 2.1 $M_\odot$ seem prone to trigger an CO explosion. Those would be natural candidates for the progenitors of supra-chandrasekhar SN Ia (Howell et al. 2006; Howell 2011), provided they are consistent with producing $\sim$ 1% of the observed type Ia systems.

3.5 Ejected mass

Previous studies of Benz et al. (1990); Segretain et al. (1997); Guerrero et al. (2004); Lorén-Aguilar et al. (2009) found ejected masses of $\sim 10^{-3}\ M_\odot$. Our large parameter space study is ideal to identify how $M_{\rm esc}$ depends on q and $M_{\rm tot}$. The fraction of ejected mass $M_{\rm esc}$, as a function of the mass ratio q, is shown in the left-side of Figure 13. We consider a particle to be unbound if the sum of its potential, kinetic and internal energy is positive. The fraction of ejecta tends to decrease with the increasing mass ratio q, and ranges between 10^{-4} and $3.4 \times 10^{-2}\ M_\odot$. Guerrero et al. (2004) also found a similar trend, though they only investigated a small fraction of the parameter space.

Very little mass leaves the system through the outer Lagrange points during the mass transfer phase, the majority becomes gravitationally unbound during the tidal disruption. At the stage shown in Figure 3, the unbound fraction does not vary anymore. It is interesting to note that in an appreciable number of cases nuclear burning substantially helps in unbinding material. These systems either go through a hydrodynamical burning phase, such as those with massive He(CO) donors, or undergo substantial nuclear burning as the very massive CO mass-transferring systems with $M_{\rm tot} \gtrsim 2.0\ M_\odot$ (Dan et al. 2012). Such systems are marked by filled, yellow circles, open circles refer to ejection purely by gravitational torques. The escaping mass from these latter systems can be estimated by means of Eq. A11, see Appendix. Although the fraction of unbound mass is relatively small, it can take up to 12% of the system's total angular momentum, see right-side of Figure 13, having an impact on the further evolution of the remnant.

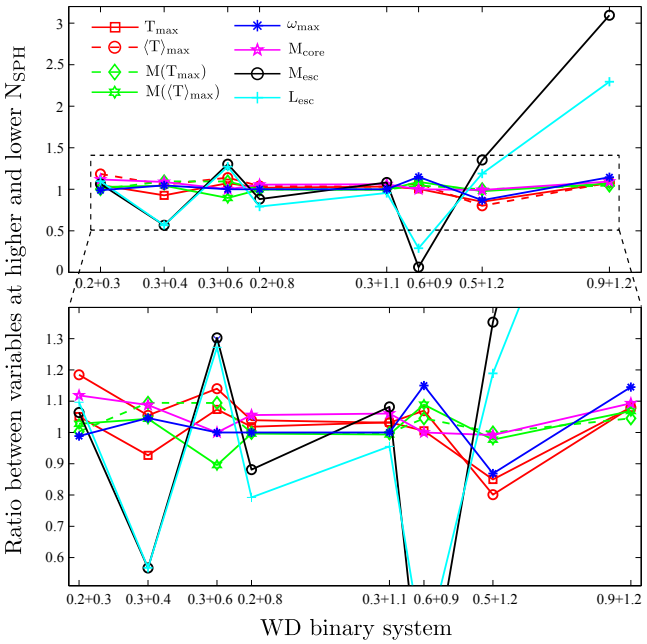

Figure 14. Ratio between different variables at $2{\times}10^5$ and $4{\times}10^4$ SPH particles runs. The runs with $2{\times}10^5$ are those from Dan et al. (2011). Most of the variables vary within 20% between higher and lower numerical resolution runs, only $M_{\rm esc}$ and $L_{\rm esc}$ are showing larger variations.

3.6 Resolution-dependence

We compared our results obtained with $4{\times}10^4$ SPH particles with the runs from Dan et al. (2011) obtained using 2×10^5 SPH particles, which corresponds to a reduction of the average resolution length by a factor of $5^{1/3} \approx 1.7$.

The variation between higher and lower numerical resolution runs does not exceed 20% for most of the variables with the exception of $M_{\rm esc}$ and $L_{\rm esc}$. The difference noted in the escape fraction of mass and angular momentum ($M_{\rm esc}$ and $L_{\rm esc}$, respectively) for the $0.6{+}0.9$ and $0.9{+}1.2\ M_\odot$ systems is due the different initial compositions that affect the nuclear burning. For the runs using 2×10^5 SPH particles presented in Dan et al. (2011) we used a different chemical composition. WDs below $0.6\ M_\odot$ are made of pure He. For $M > 0.6\ M_\odot$ we have chosen mass fractions $\mathrm{X}(^{12}\mathrm{C}) = 0.5$ and $\mathrm{X}(^{16}\mathrm{O}) = 0.5$ uniformly distributed throughout the star, with the exception of the $0.5 + 1.2\ M_\odot$ system which has an ONeMg composition, as in the current study. For example, if we take the run with $0.9 + 1.2\ M_\odot$ from Dan et al. (2011) we find that the nuclear energy produced by C-burning is about 5 times larger compared to the current study. As discussed in §3.5, the fraction of unbound mass and angular momentum increases for the runs that undergo dynamical burning or substantial burning.

We therefore conclude that our results are not fully converged, but the trends we found should be robust. Effects related to nuclear burning may be seriously underestimated due to the low numerical resolutions.

3.7 Comparison with other work

While finishing this paper, a preprint by Zhu et al. (2013) appeared, which explores the parameter space of the CO WD mergers. They discuss the structure of similar- and dissimilar-mass mergers and provide detailed information on the remnants' main properties. The differences between our and their calculations are the following: (i) we are using tidally locked stars while they start with non-spinning stars at an initial separation obtained from an estimate of the size of the Roche lobe (Eggleton 1983); (ii) we are including feedback from the nuclear burning and (iii) we cover the full parameter space of both He(CO) and CO donors while they focus on the CO donors.

As a proxy to indicate where ignition is most likely, we compare the enclosed mass at the location where $T = \langle T\rangle_{\rm max}$, $M(\langle T\rangle_{\rm max})$, see Figure 15 (left panel) and the location where the angular velocity is half the Keplerian value, $M(\omega = \omega_K/2)$. This location corresponds to the inner/outer edge of the disk/core in Zhu et al. (2013), see Figure 15 (right panel). As in Zhu et al. (2013) we are using the density ratio $q_\rho = \rho_{\rm don,0}/\rho_{\rm acc,0}$, where $\rho_{\rm don,0}$ and $\rho_{\rm acc,0}$ are the central densities at the moment when mass transfer sets in for the donor and the accretor, respectively.

In accordance with Zhu et al. (2013), we found that the fraction of the core that is heated up increases with the

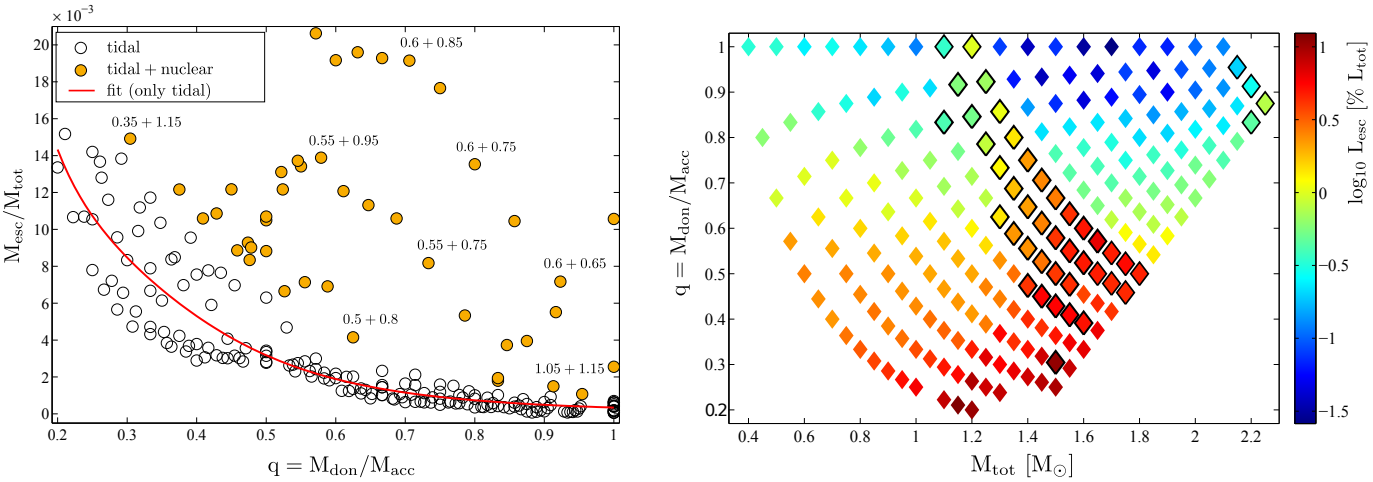

Figure 13. Left: ejected mass fraction as a function of the mass ratio $q = M_{\rm don}/M_{\rm acc}$. In a number of cases, nuclear burning has a substantial impact on ejecting mass. Such systems are marked by filled, yellow circles. Matter that is predominantly ejected by gravitational torques can be fit by Equation A11. This fit is shown by the red line. To provide a visual aid, few of these systems have been labeled. Right: the fraction of angular momentum contained in material that is unbound in the $q - M_{\rm tot}$ plane. The amount of ejected mass is tiny, up to 2% of the total mass, but this can take up to 10% of the total angular momentum. The systems that have not been used in the fit $M_{\rm esc}(q)$ are marked with slightly larger symbols and with a black stroke. Most of the mass is ejected during the tidal disruption, although a small fraction leaves the system through the outer Lagrange points during the mass transfer phase.

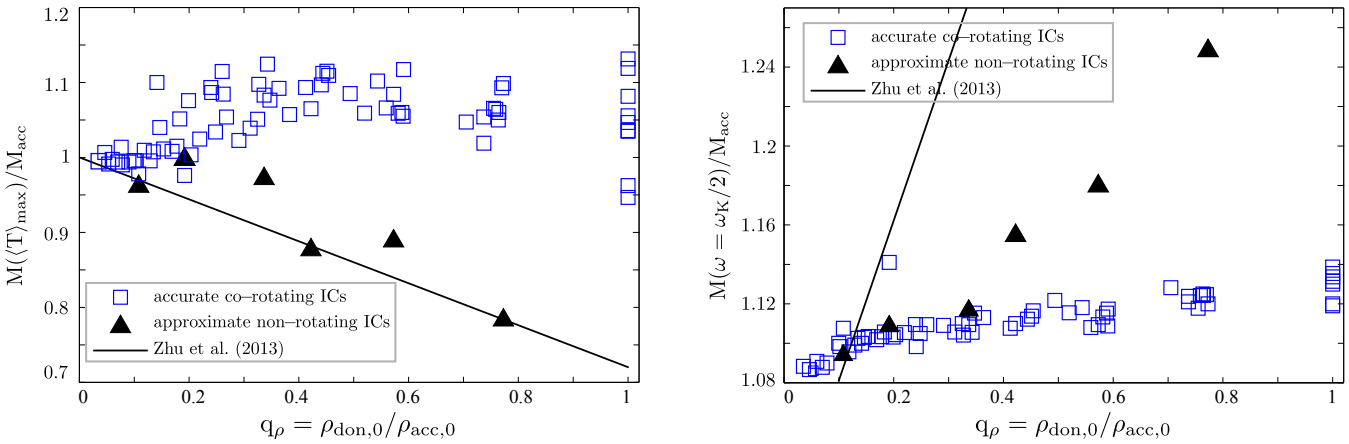

Figure 15. Comparison with Zhu et al. (2013) for the CO mass-transferring systems: (left) enclosed mass at the location of maximum temperature $M(\langle T\rangle_{\rm max})$; (right) location in mass coordinate where $\omega = \omega_{\rm K}/2$, $M(\omega = \omega_{\rm K}/2)$. The black triangles mark the results obtained using the "approximate" non rotating ICs. The masses are scaled in terms of the accretor's mass and plotted against the density ratio $q_\rho = \rho_{\rm don,0}/\rho_{\rm acc,0}$. The continuous lines are fits to the data and the dashed lines are the fits found by Zhu et al. (2013).

mass ratio. However, when comparing the location in mass coordinate of the peak temperature our results do not agree. As we have shown in Section 3.2, the difference between our and Zhu et al. (2013) is caused by the different ICs. In the non-rotating case, the peak temperature occurs closer to the center of the remnant as the mass ratio increases and that for nearly equal-mass components both stars are symmetrically disrupted. In contrast, in the corotating case the locations of maximum temperature are located at the surface rather than the centre of the high-density core. To test the trends obtained by Zhu et al. (2013), we followed the evolution of six systems with density ratios ranging between 0.1 and 0.8 using non-rotating ICs (represented with black triangles in Figure 15). Our results from the runs with non-rotating ICs confirm the results of Zhu et al. (2013).

The location in mass coordinate where $\omega = \omega_K/2$ is more similar with Zhu et al. (2013), increasing with the mass (density) ratio, although the function obtained by Zhu et al. (2013) has a steeper slope. This is again attributed to the different ICs as the corotating ICs start with more angular momentum compared to non-rotating ICs. The results for the non-rotating ICs are over-plotted with black triangles and match better the fitted formula of Zhu et al. (2013). Note that the angular velocity and temperature are averaged differently. In our study they are averaged over equipotential surfaces, while in Zhu et al. (2013) they are cylindrically

averaged. Moreover, the enclosed mass is defined differently, in Zhu et al. (2013) within spherical radii, while in our case within equipotential surfaces.

As stated before, it is not well known whether the binary systems realized in nature are synchronized or not. If they are, off centre ignitions at moderate densities ($\sim 10^5$ g cm^{-3}) are likely. If instead they are not synchronized, dynamical burning may start deep in the remnant core, which, due to faster reaction rate, may lead to a more robust explosion mechanism.

4 APPLICATIONS

Our simulations have direct applications to a number of observed stellar systems and events, such as hot subdwarfs, RCB stars, single massive white dwarfs, supernovae and other transient events.

4.1 Hot subdwarfs ($M_{\rm tot} \lesssim 0.8\,M_\odot$)

Mergers that contain at least one He WD and whose combined mass is larger than $\sim 0.38 - 0.45\,M_\odot$ (depending on the mass of the more massive WD; Han et al. 2003) will ignite He, generally in a shell, and experience a series of He shell flashes that propagate inwards (in the case of two He WD) until helium burns in the core (Saio & Jeffery 2000). During these He shell flashes, the envelope expands and may attain giant dimensions, temporarily resembling an RCB star (Saio & Jeffery 2000; Justham et al. 2011). Once helium burns steadily in the core (for $\sim 10^8$ yr), the merged object will be relatively compact (with a radius $\sim 0.1\,R_\odot$) and have the appearance of a hot subdwarf. If the mass of the merger product is $\lesssim 0.8\,M_\odot$ (see, e.g., Paczyński 1971; Iben & Tutukov 1985), the object will remain compact after He core burning and ultimately become a WD, a hybrid HeCO WD with a substantial He envelope (Iben & Tutukov 1985).

The merger of two He WDs is believed to be the main channel to produce single sdB stars with a typical Galactic formation rate of $0.1\,{\rm yr}^{-1}$ (e.g. Tutukov & Yungelson 1990; Nelemans et al. 2001; Han et al. 2003). If the merger involves one (or possibly two) HeCO WDs, the merger product will generally be more massive and hotter. These merger products are excellent candidates for He-rich sdO stars (Stroeer et al. 2007; Justham et al. 2011) and may make up up to $\sim 10\,\%$ of the subdwarf population (Nelemans et al. 2001; Justham et al. 2011). Interestingly, Stroeer et al. (2007) find that He-rich sdO stars come in different varieties and can be C and/or N-rich, perhaps indicating different merger histories.

4.2 RCB and EHe stars ($0.8 \lesssim M_{\rm tot}/M_\odot \leqslant 1.4$)

Merger products that contain a CO core and a He-rich layer and have a mass larger than $\sim 0.8\,M_\odot$ will expand and become He giants (Paczyński 1971; Iben & Tutukov 1985). This is believed to be the main channel to produce extreme He stars (EHe stars) and RCB stars (Webbink 1984; Iben & Tutukov 1985). Our simulations show that there are at least two different channels to produce such objects with very different chemical profiles and surface abundances. The merger of a He + CO WD (the "classical" channel to produce RCB stars with an estimated Galactic birth rate of $\sim 0.01\,{\rm yr}^{-1}$; e.g., Iben et al. 1996; Han 1998) leads to a He-shell burning star with a massive He envelope but low C and O abundance. In contrast, the merger of a CO WD and a HeCO WD (and possibly the merger of two HeCO WDs) produces an object with a large surface overabundance of C and O (see Figure 11). This may explain the large observed abundances of C and O in EHe stars (Pandey et al. 2001; Saio & Jeffery 2002, and to a similar, but somewhat lower extent in RCB stars;) without requiring extreme mixing in the progenitor of the CO WD on the asymptotic giant branch (cf. Herwig 2000; also see Menon et al. 2013). Indeed, different merger histories could account, at least in part, for the apparent differences in the surface abundances of EHe and RCB stars (see the discussions in Pandey et al. 2001; Saio & Jeffery 2002).

4.3 Massive single white dwarfs ($M_{\rm tot} \leqslant 1.4\,M_\odot$)

The merger of two CO WDs with a combined mass below the Chandrasekhar limit is expected to lead to the formation of a single CO white dwarf, (assuming that carbon is not ignited in the merger event; see § 4.5). The resulting WD may be substantially more massive than any CO WD that can form from a single star ($\sim 1.1\,M_\odot$). An excellent candidate is the rapidly rotating WD RE J0317-853 (Barstow et al. 1995) which appears to have a mass close to the Chandrasekhar mass (Külebi et al. 2010). RE J0317-853 is also one of the most magnetic WDs known. This could be a direct consequence of the merger process in which differential rotation may drive a magnetic dynamo amplifying any seed magnetic field (also see Tout et al. 2008).

4.4 Helium detonations and sub-Chandrasekhar explosions ($M_{\rm tot} \leqslant 1.4\,M_\odot$)

Many of our simulations that contain a He-rich WD achieve conditions in the ρ–T plane where helium may be expected to detonate (see Fig. 12). This can lead to a rather bright explosion and could easily be mistaken for a faint supernova (Nomoto 1982b). Indeed, as such detonations produce elements similar to a SN Ia, they may resemble a faint SN Ia and are therefore sometimes referred to as SNe .Ia (Bildsten et al. 2007). The main difference is that the underlying CO white dwarf is likely to survive. On the other hand, if the helium detonation drives a sufficiently strong shock into the CO core, this could trigger a second detonation near the core, a carbon detonation, which would then destroy the whole white dwarf and produce a SN Ia-like event. Such double-detonation models are a possible scenario for sub-Chandrasekhar SNe Ia (Woosley & Weaver 1994; Fink et al. 2010). Even though such double detonations are only likely to occur for the more massive merger products (see Figure 12), they are sufficiently common that they could

easily produce a large fraction, if not all, SNe Ia. One problem with this scenario is that the simulated spectra (Kromer et al. 2010), using standard assumptions, are too red to be consistent with observed SNe Ia. However, Kromer et al. (2010) also show that this problem could be solved if the He layer contained a large amount of carbon ($\sim 34\,\%$ by mass). Interestingly, this is close to the C abundance found in our simulations in the outer He-rich layer if the merger involves a hybrid HeCO WD (see Figure 11), perhaps providing some support for the Kromer et al. (2010) suggestion.

4.5 CO + CO WD mergers: SN Ia or AIC ($M_{\rm tot} > 1.4\,M_{\odot}$)

The mergers of two CO WDs with a total mass above the Chandrasekhar mass limit is one of the main channels to produce a Type Ia supernova (SN Ia) (Iben & Tutukov 1984; Webbink 1984).

However, it has been argued that in the WD merger scenario off-center C burning transforms the CO WD into an ONeMg WD that will undergo accretion induced collapse (AIC) to form a neutron star (Nomoto & Iben 1985). Yoon et al. (2007) found (cf. § 3.4) that there may be some parameter range for which neutrino cooling prevents the conversion of the CO WD into an ONeMg WD; in this case, carbon will be ignited in the center, leading to a SN Ia, $\sim 10^5$ yr after the merger itself.

In the case of nearly equal mass CO WDs, where both WDs are disrupted and merge, C may detonate in the merging process (Pakmor et al. 2010). In our simulations, unlike those by Pakmor et al. (2010), this is only likely to happen for the most massive WDs (see Figure 12) because of the different initial assumed WD spins (see the discussion in § 3.2). The most massive mergers (with $M_{\rm tot} \geqslant 2.1\,M_{\odot}$) may detonate during the merger and therefore are potential candidates to explain the so-called super-Chandrasekhar SN Ia explosions, which are much brighter than normal SNe Ia (e.g., SNLS-03D3bb, Howell et al. 2006). As such massive systems will be rare, this would naturally explain their low observed frequency.

4.6 Hybrid supernovae ($M_{\rm tot} > 1.4\,M_{\odot}$)

Our simulations also include cases where the combined mass exceeds the Chandrasekhar mass but does not involve two CO WDs. In cases, where at least one of the WDs contains a He-rich layer, it is possible, perhaps even likely, that the He detonates leading to the ejection of this layer (see Figure 12 and § 4.4). In cases where the post-merger object remains above the Chandrasekhar mass, it will ultimately experience a SN (e.g. Iben & Tutukov 1985), either a thermonuclear explosion (if C is ignited in the centre) or core collapse (in the case of an ONeMg core). This may give rise to new types of supernova events. For example, in the case of the collapse of an ONeMg core to a neutron star with a significant He layer, the explosion would technically be a core-collapse supernova, but as such explosions (initiated by the capture of electrons onto Ne and Mg Nomoto 1984) are expected to be weak (Podsiadlowski et al. 2004; Kitaura et al. 2006), most of the explosion energy may come from He burning, i.e., be thermonuclear in nature. Such hybrid supernovae (observationally classified as a weak SN Ib) are potential candidates for the class of "Ca-rich" SNe Ib (such as SN 2005E Perets et al. 2010) as the burning conditions are likely to favor the production of intermediate-mass elements (e.g. Waldman et al. 2011)[1]. Ca-rich SNe as a class are preferentially found in the outer parts of galaxies, far away from star-forming regions, implying old and possibly metal-poor progenitor systems (Yuan et al. 2013). This could be consistent with a merger origin if the merger requires a long time delay to bring the systems into contact.

The merger of a CO and ONeMg WD could be another hybrid SN, where the ONeMg core may collapse but carbon may or may not detonate. Depending on the details, this could lead to either an unusual SN Ia or a (faint?) SN Ic. Such mergers will be rare but should exist in nature.

5 SUMMARY

In this paper, we have investigated the merger properties of more than 200 WD-WD systems covering a large range of WD mass and chemical compositions. We have determined the structure of the WD remnants as a function of the total mass and the mass ratio of the binary. We distinguish between four main regions: a cold core surrounded by a hot, thermally supported envelope, a Keplerian disk and a tidal tail. The degree of heating experienced by the accretor is closely related to the degree of mixing of the two stars, both increasing with the mass ratio. Consequently, the fraction of the accretor that remains cold (core) tends to decrease with increasing mass ratio while the fraction of mass outside this region (combined mass of the hot envelope and the centrifugally supported disk) tends to increase with the mass ratio. Systems with lower mass ratio have more total angular momentum and as a result more mass is flung out in a tidal tail. Most of this material will fall back at a later time onto the disk.

However, the remnant's structure is strongly dependent on the nature of the initial conditions. We made a detailed comparison with the previous parameter study of CO mass-transferring systems of Zhu et al. (2013) and found that the differences in the remnants' structure are due to the different initial conditions. When using the non-rotating initial stars as in Zhu et al. (2013), we found that for nearly equal mass mergers both stars are symmetrically disrupted and the location of peak temperature is at the remnant's center. With our corotating initial conditions the location of peak temperature is close (within 15 %) to the surface of the former accretor. The initial conditions are also responsible for the difference found in the rotational profiles, the corotating the initial conditions lead to more angular momentum in the central remnant compared to the non-rotating the initial conditions.

[1] He detonations on a CO or ONeMg core themselves provide an alternative scenario for this supernova type (Waldman et al. 2011).

Little mass is ejected, between 10^{-4} and $3.4 \times 10^{-2}\,M_\odot$ as the mass ratio decreases. However, this can take up to 12 % of the system's total angular momentum having an impact on the post-merger viscous evolution. In an appreciable number of cases, nuclear burning has a substantial impact on ejected mass. These systems undergo substantial nuclear burning, such as those with massive He(CO) donors or the very massive CO mass-transferring systems with $M_{\rm tot} \gtrsim 2.0\,M_\odot$.

We investigated whether hydrodynamical burning can occur after the merger moment. Many of our simulations ($M_{\rm tot} \gtrsim 1.1\,M_\odot$) that contain a He-rich WD achieve the conditions required to trigger a He detonation. These are roughly the same systems that are expected to produce surface detonations either from instabilities within the accretion stream and/or at the moment first dynamical contact (Guillochon et al. 2010; Dan et al. 2012). Further viscous evolution could possibly increase the region of parameter space in which one expects a detonation to occur (Schwab et al. 2012). The He-detonations may resemble a SN Ia, but in this case the underlying CO white dwarf can survive. If the He shock can trigger a second detonation in the CO core, then the whole white dwarf is disrupted and will produce a SN Ia-like event.

For our CO mass-transferring systems only the most massive mergers ($M_{\rm tot} \gtrsim 2.1\,M_\odot$) may detonate. These systems are potential candidates to explain the so-called super-Chandrasekhar SN Ia explosions, which are much brighter than normal SNe Ia. However, even systems with lower masses may still be prone to an explosion long after the merger if the post-merger object remains above the Chandrasekhar mass (e.g. Iben & Tutukov 1985; Yoon et al. 2007) and C is ignited in the centre. Alternatively, off center ignition of C burning transforms the CO WD into an ONeMg WD that will undergo accretion induced collapse (AIC) to form a neutron star (Nomoto & Iben 1985).

Finally, we provide to the astrophysical community a large database containing thermodynamic and rotational profiles to be used for subsequent stellar evolution studies. The data from our large simulation set can be downloaded from `www.hs.uni-hamburg.de/DE/Ins/Per/Dan/wdwd_remnants`. In order to aid further comparisons, the general remnants properties are tabulated, see Table A1 in the Appendix.

ACKNOWLEDGMENTS

We thank Enrico Ramirez-Ruiz and James Guillochon for very useful discussions. M.D. and S.R. are supported by Deutsche Forschungsgemeinschaft under grants RO-3399/4-1 and RO-3399/4-2. M.B. acknowledges computing on the JUROPA supercomputer at the Forschungszentrum Jülich under grant NIC5984 and 5056. Some of the figures in this paper were produced using the visualization software SPLASH developed by Daniel Price (2007).

REFERENCES

Amaro-Seoane P. et al., 2012, Classical and Quantum Gravity, 29, 124016
Balsara D. S., 1995, Journal of Computational Physics, 121, 357
Barstow M. A., Jordan S., O'Donoghue D., Burleigh M. R., Napiwotzki R., Harrop-Allin M. K., 1995, MNRAS, 277, 971
Benz W., Cameron A. G. W., Press W. H., Bowers R. L., 1990, ApJ, 348, 647
Bergeron P., Kidder K. M., Holberg J. B., Liebert J., Wesemael F., Saffer R. A., 1991, ApJ, 372, 267
Bildsten L., Shen K. J., Weinberg N. N., Nelemans G., 2007, ApJL, 662, L95
Blinnikov S. I., Khokhlov A. M., 1987, Soviet Astronomy Letters, 13, 364
Brown W. R., Kilic M., Hermes J. J., Allende Prieto C., Kenyon S. J., Winget D. E., 2011, ApJL, 737, L23
Burkart J., Quataert E., Arras P., Weinberg N. N., 2012, ArXiv e-prints
Clayton D. D., 1968, Principles of stellar evolution and nucleosynthesis
Clayton G. C., 2012, Journal of the American Association of Variable Star Observers (JAAVSO), 40, 539
Dan M., Rosswog S., Guillochon J., Ramirez-Ruiz E., 2011, ApJ, 737, 89
Dan M., Rosswog S., Guillochon J., Ramirez-Ruiz E., 2012, MNRAS, 422, 2417
Eggleton P. P., 1983, ApJ, 268, 368
Fink M., Röpke F. K., Hillebrandt W., Seitenzahl I. R., Sim S. A., Kromer M., 2010, A&A, 514, A53
Fowler W. A., Caughlan G. R., Zimmerman B. A., 1975, ARA&A, 13, 69
Frank-Kamenetskii D., 1967, Diffusion and Heat Transfer in Chemical Kinetic. Nauka, Moscow
Fryer C. L. et al., 2010, ApJ, 725, 296
Fuller J., Lai D., 2012, MNRAS, 421, 426
Gokhale V., Peng X. M., Frank J., 2007, ApJ, 655, 1010
Guerrero J., García-Berro E., Isern J., 2004, A&A, 413, 257
Guillochon J., Dan M., Ramirez-Ruiz E., Rosswog S., 2010, ApJL, 709, L64
Han Z., 1998, MNRAS, 296, 1019
Han Z., Podsiadlowski P., Maxted P. F. L., Marsh T. R., 2003, MNRAS, 341, 669
Han Z., Podsiadlowski P., Maxted P. F. L., Marsh T. R., Ivanova N., 2002, MNRAS, 336, 449
Heber U., 2009, ARA&A, 47, 211
Herwig F., 2000, A&A, 360, 952
Hix W. R., Khokhlov A. M., Wheeler J. C., Thielemann F.-K., 1998, ApJ, 503, 332
Howell D. A., 2011, Nature Communications, 2
Howell D. A. et al., 2006, Nature, 443, 308
Iben, Jr. I., Tutukov A. V., 1984, ApJS, 54, 335
Iben, Jr. I., Tutukov A. V., 1985, ApJS, 58, 661
Iben, Jr. I., Tutukov A. V., Yungelson L. R., 1996, ApJ, 456, 750
Jeffery C. S., Karakas A. I., Saio H., 2011, MNRAS, 414, 3599

Justham S., Podsiadlowski P., Han Z., 2011, MNRAS, 410, 984
Kilic M., Brown W. R., Allende Prieto C., Agüeros M. A., Heinke C., Kenyon S. J., 2011, ApJ, 727, 3
Kippenhahn R., Weigert A., 1990, Stellar Structure and Evolution
Kitaura F. S., Janka H.-T., Hillebrandt W., 2006, A&A, 450, 345
Kromer M., Sim S. A., Fink M., Röpke F. K., Seitenzahl I. R., Hillebrandt W., 2010, ApJ, 719, 1067
Külebi B., Jordan S., Nelan E., Bastian U., Altmann M., 2010, A&A, 524, A36
Lorén-Aguilar P., Isern J., García-Berro E., 2009, A&A, 500, 1193
Marsh T. R., 2011, Classical and Quantum Gravity, 28, 094019
Marsh T. R., Nelemans G., Steeghs D., 2004, MNRAS, 350, 113
Menon A., Herwig F., Denissenkov P. A., Clayton G. C., Staff J., Pignatari M., Paxton B., 2013, ApJ, 772, 59
Monaghan J. J., 2005, Reports on Progress in Physics, 68, 1703
Morris J. P., Monaghan J. J., 1997, Journal of Computational Physics, 136, 41
Napiwotzki R., 2009, Journal of Physics Conference Series, 172, 012004
Napiwotzki R. et al., 2004, in Astronomical Society of the Pacific Conference Series, Vol. 318, Spectroscopically and Spatially Resolving the Components of the Close Binary Stars, Hilditch R. W., Hensberge H., Pavlovski K., eds., pp. 402–410
Nelemans G., 2005, in Astronomical Society of the Pacific Conference Series, Vol. 330, The Astrophysics of Cataclysmic Variables and Related Objects, J.-M. Hameury & J.-P. Lasota, ed., p. 27
Nelemans G., 2009, Classical and Quantum Gravity, 26, 094030
Nelemans G., Yungelson L. R., Portegies Zwart S. F., Verbunt F., 2001, A&A, 365, 491
Nomoto K., 1982a, ApJ, 257, 780
Nomoto K., 1982b, ApJ, 253, 798
Nomoto K., 1984, ApJ, 277, 791
Nomoto K., Iben, Jr. I., 1985, ApJ, 297, 531
Nomoto K., Kondo Y., 1991, ApJL, 367, L19
Paczyński B., 1971, Acta Astronomica, 21, 1
Pakmor R., Hachinger S., Röpke F. K., Hillebrandt W., 2011, A&A, 528, A117+
Pakmor R., Kromer M., Röpke F. K., Sim S. A., Ruiter A. J., Hillebrandt W., 2010, Nature, 463, 61
Pandey G., Kameswara Rao N., Lambert D. L., Jeffery C. S., Asplund M., 2001, MNRAS, 324, 937
Parsons S. G., Marsh T. R., Gänsicke B. T., Drake A. J., Koester D., 2011, ApJL, 735, L30
Perets H. B. et al., 2010, Nature, 465, 322
Podsiadlowski P., Langer N., Poelarends A. J. T., Rappaport S., Heger A., Pfahl E., 2004, ApJ, 612, 1044
Price D. J., 2007, PASA, 24, 159
Price D. J., Rosswog S., 2006, Science, 312, 719
Rasio F. A., Shapiro S. L., 1999, Classical and Quantum Gravity, 16, 1
Raskin C., Scannapieco E., Fryer C., Rockefeller G., Timmes F. X., 2011, ArXiv e-prints
Rosswog S., 2007, MNRAS, 376, L48
Rosswog S., 2009, NewAR, 53, 78
Rosswog S., Davies M. B., 2002, MNRAS, 334, 481
Rosswog S., Davies M. B., Thielemann F.-K., Piran T., 2000, A&A, 360, 171
Rosswog S., Kasen D., Guillochon J., Ramirez-Ruiz E., 2009a, ApJL, 705, L128
Rosswog S., Liebendörfer M., Thielemann F., Davies M. B., Benz W., Piran T., 1999, A&A, 341, 499
Rosswog S., Piran T., Nakar E., 2013, MNRAS, 430, 2585
Rosswog S., Ramirez-Ruiz E., Hix W. R., 2009b, ApJ, 695, 404
Rosswog S., Ramirez-Ruiz E., Hix W. R., Dan M., 2008, Computer Physics Communications, 179, 184
Rosswog S., Speith R., Wynn G. A., 2004, MNRAS, 351, 1121
Ruffert M., Janka H.-T., Schaefer G., 1996, A&A, 311, 532
Saio H., Jeffery C. S., 2000, MNRAS, 313, 671
Saio H., Jeffery C. S., 2002, MNRAS, 333, 121
Saio H., Nomoto K., 1985, A&A, 150, L21
Saio H., Nomoto K., 2004, ApJ, 615, 444
Salpeter E. E., 1954, Australian Journal of Physics, 7, 373
Schwab J., Shen K. J., Quataert E., Dan M., Rosswog S., 2012, MNRAS, 427, 190
Segretain L., Chabrier G., Mochkovitch R., 1997, ApJ, 481, 355
Shen K. J., Kasen D., Weinberg N. N., Bildsten L., Scannapieco E., 2010, ApJ, 715, 767
Sim S. A., Röpke F. K., Hillebrandt W., Kromer M., Pakmor R., Fink M., Ruiter A. J., Seitenzahl I. R., 2010, ApJL, 714, L52
Steinfadt J. D. R., Kaplan D. L., Shporer A., Bildsten L., Howell S. B., 2010, ApJL, 716, L146
Stroeer A., Heber U., Lisker T., Napiwotzki R., Dreizler S., Christlieb N., Reimers D., 2007, A&A, 462, 269
Taam R. E., 1980, ApJ, 237, 142
Timmes F. X., Swesty F. D., 2000, ApJS, 126, 501
Tout C. A., Wickramasinghe D. T., Liebert J., Ferrario L., Pringle J. E., 2008, MNRAS, 387, 897
Tutukov A. V., Yungelson L. R., 1990, A. Zh., 67, 109
van Kerkwijk M. H., Chang P., Justham S., 2010, ApJL, 722, L157
Vennes S. et al., 2011, ApJL, 737, L16
Waldman R., Sauer D., Livne E., Perets H., Glasner A., Mazzali P., Truran J. W., Gal-Yam A., 2011, ApJ, 738, 21
Webbink R. F., 1984, ApJ, 277, 355
Woosley S. E., Kasen D., 2011, ApJ, 734, 38
Woosley S. E., Weaver T. A., 1994, ApJ, 423, 371
Yoon S., Podsiadlowski P., Rosswog S., 2007, MNRAS, 380, 933
Yuan F., Kobayashi C., Schmidt B. P., Podsiadlowski P., Sim S. A., Scalzo R. A., 2013, MNRAS, 432, 1680
Zhu C., Chang P., van Kerkwijk M. H., Wadsley J., 2013, ApJ, 767, 164
Zrake J., MacFadyen A. I., 2013, ArXiv e-prints

APPENDIX A: POLYNOMIAL FITTING FUNCTIONS

We provide approximate formulae for $M(T_{\max})$, $M(\langle T\rangle_{\max})$, $M(\omega_{\max})$, $M(\omega_k/2)$, $M_{\rm core}$, $M_{\rm env}$, $M_{\rm disk}$, $M_{\rm fb}$, and $M_{\rm esc}$ as a function of q and $M_{\rm tot}$, valid for the entire parameter space under study, ie. both He and CO mass-transferring systems.

To measure the goodness of the fit of the estimated equations we use the R^2 statistic, defined as the ratio of the sum of squares of the residuals and the total sum of squares. R^2 can take values between 0 and 1 and the closer is to 1 the better the fit. For example, an R^2 value of 0.7 means that the fit explains 70% of the variance.

$$M(T_{\max}) = M_{\rm tot}(0.863 - 0.3335q) \quad \text{(A1)}$$

$$M(\langle T\rangle_{\max}) = M_{\rm tot}(0.851 - 0.319q), \quad \text{(A2)}$$

having an R^2 goodness-of-fit of 0.75 and 0.85, respectively.

$$\omega_{\max} = \omega_{\rm orb,0}(-3.476q + 6.148), \quad \text{(A3)}$$

with R^2 equal to 0.6012.

$$M(\omega_{\max}) = M_{\rm tot}(0.8684 - 0.3284q). \quad \text{(A4)}$$

The R^2 goodness-of-fit is equal to 0.92 if we exclude seven runs ($0.2{+}0.7\,M_\odot$, $0.2{+}0.9\,M_\odot$,$0.2{+}0.95\,M_\odot$, $0.25{+}0.7\,M_\odot$, $0.25 + 0.8\,M_\odot$, $0.3 + 0.85\,M_\odot$, $0.7 + 1\,M_\odot$) that have $\omega_{\max}$ close to the accretor's center of mass.

$$M_{\rm core} = M_{\rm tot}(0.7786 - 0.5114q) \quad \text{(A5)}$$

$$M_{\rm env} = M_{\rm tot}(0.2779 - 0.464q + 0.7161q^2) \quad \text{(A6)}$$

$$M_{\rm disk} = M_{\rm tot}(-0.1185 + 0.9763q - 0.6559q^2) \quad \text{(A7)}$$

$$M_{\rm fb} = M_{\rm tot}(0.07064 - 0.0648q), \quad \text{(A8)}$$

with R^2 equal to 0.97, 0.88, 0.78 and 0.8, respectively.

In order to compare with Zhu et al. (2013) we also provide the fitting formula for $M(T_{\max})$ and $M(\omega = \omega_{\rm K}/2)$ with respect to $q_\rho = \rho_{\rm don,0}/\rho_{\rm acc,0}$ and $M_{\rm acc}$, where $\rho_{\rm don,0}$ and $\rho_{\rm acc,0}$ are the initial central density of the donor and accretor, respectively, for the systems with CO donors. For additional information about our comparison with Zhu et al. (2013), see Section 3.7.

$$M(\langle T_{\max}\rangle) = M_{\rm acc}(0.952 + 0.65q_\rho - 0.9945q_\rho^2 + 0.4378q_\rho^3) \quad \text{(A9)}$$

$$M(\omega = \omega_{\rm K}/2) = M_{\rm tot}(1.095 + 0.03784q_\rho), \quad \text{(A10)}$$

with R^2 equal to 0.45 and 0.73, respectively.

This rational polynomial for the unbound fraction of mass $M_{\rm esc}$ as a function of $M_{\rm tot}$ and q was obtained by excluding most of the systems that reach, or are very close to the conditions for dynamical burning (as obtained in Dan et al. 2012), see Figure 13 where we marked these systems.

$$M_{\rm esc} = M_{\rm tot}\frac{0.0001807}{-0.01672 + 0.2463q - 0.6982q^2 + q^3}. \quad \text{(A11)}$$

APPENDIX B: SUMMARY OF WHITE DWARF MERGER REMNANTS

Detailed instructions how to read the data in the remnant structure profiles made available through `www.hs.uni-hamburg.de/DE/Ins/Per/Dan/wdwd_remnants` are included on the website.

The quantities presented in the following table are: P_0 is the initial orbital period in seconds; $T_{\max}$ is the peak temperature and $\langle T\rangle_{\max}$ is the SPH-smoothed peak temperature, both in units of 10^8 K; $\rho(T_{\max})$ and $\rho(\langle T\rangle_{\max})$ are the densities at the location of $T_{\max}$ and $\langle T\rangle_{\max}$, respectively, in units of 10^3 g cm^{-3}; $\rho_{\max}$ is the peak density in units of 10^6 g cm^{-3}; $M(T_{\max})$ and $M(\langle T\rangle_{\max})$ are the enclosed mass at the location of peak temperature $T_{\max}$ and $\langle T\rangle_{\max}$, respectively, in units of $M_\odot$; $\omega_{\max}$ is the peak value of the averaged (over equipotential surfaces) angular velocity and $M(\omega_{\max})$ is the corresponding location in mass coordinate. $M_{\omega_k/2}$ is the location in mass coordinate where the angular velocity equals half the Keplerian value. $M_{\rm core}$, $M_{\rm env}$ and $M_{\rm disk}$ are the masses of the central (isothermal) core, the hot envelope and the (nearly) Keplerian disk, respectively, in units of $M_\odot$; $M_{\rm fb}$ is the mass of the tidal tail that is falling back onto the central remnant in units of $10^{-2}\,M_\odot$; $M_{\rm esc}$ is the escape fraction of mass in units of $10^{-3}\,M_\odot$; $L_{\rm esc}$ is the fraction of angular momentum contained in material that is unbound. Enclosed masses are computed with respect to the accretors center of mass and defined within equipotential surfaces.

Table A1: Summary of the runs performed for this paper.

$M_{\rm don}$ $M_\odot$	$M_{\rm acc}$ $M_\odot$	P_0 s	$\rho_{\rm max}$ 10^6 g/cm^3	$T_{\rm max}$ 10^8 K	$\rho(T_{\rm max})$ 10^3 g/cm^3	$M(T_{\rm max})$ $M_\odot$	$\langle T\rangle_{\rm max}$ 10^8 K	$\rho(\langle T\rangle_{\rm max})$ 10^3 g/cm^3	$M(\langle T\rangle_{\rm max})$ $M_\odot$	$\omega_{\rm max}$ rad/s	$M(\omega_{\rm max})$ $M_\odot$	$M(\omega_{\rm k}/2)$ $M_\odot$	$M_{\rm core}$ $M_\odot$	$M_{\rm env}$ $M_\odot$	$M_{\rm disk}$ $M_\odot$	$M_{\rm fb}$ $10^{-2}M_\odot$	$M_{\rm esc}$ $10^{-3}M_\odot$	$L_{\rm esc}$ $\%L_{\rm tot}$	Outcome
Helium – Helium																			
0.2	0.2	215.249	0.203	0.414	0.326	0.322	0.285	6.394	0.269	0.076	0.210	0.230	0.107	0.225	0.059	0.873	0.244	0.331	
0.2	0.25	216.726	0.328	0.569	3.023	0.304	0.481	6.834	0.285	0.081	0.289	0.280	0.148	0.207	0.088	0.741	0.452	0.600	
0.2	0.3	207.567	0.484	0.785	4.571	0.347	0.602	12.051	0.327	0.087	0.336	0.334	0.211	0.181	0.098	0.965	0.720	0.942	
0.2	0.35	229.584	0.691	1.033	2.087	0.406	0.822	7.873	0.381	0.089	0.376	0.391	0.259	0.162	0.111	1.627	1.648	2.200	
0.2	0.4	226.102	0.951	1.245	4.078	0.438	1.012	2.944	0.445	0.096	0.431	0.440	0.324	0.147	0.104	2.226	2.054	2.626	
0.2	0.45	232.394	1.283	1.597	3.843	0.486	1.213	2.831	0.493	0.105	0.481	0.487	0.352	0.154	0.091	5.153	1.961	2.395	
0.25	0.25	169.393	0.334	0.530	1.675	0.351	0.395	22.371	0.300	0.097	0.265	0.286	0.125	0.278	0.090	0.615	0.308	0.339	
0.25	0.3	170.515	0.504	0.769	12.493	0.360	0.601	15.577	0.333	0.103	0.342	0.336	0.173	0.255	0.113	0.886	0.559	0.590	
0.25	0.35	170.383	0.721	0.974	6.324	0.411	0.778	14.021	0.390	0.109	0.398	0.389	0.231	0.211	0.143	1.376	0.934	0.993	
0.25	0.4	175.930	0.986	1.216	8.652	0.444	0.992	6.422	0.453	0.113	0.442	0.446	0.285	0.193	0.157	1.422	1.312	1.427	
0.25	0.45	174.924	1.321	1.446	15.918	0.485	1.180	5.106	0.503	0.119	0.487	0.497	0.348	0.187	0.138	2.506	1.992	2.057	
0.3	0.3	135.734	0.516	0.770	103.478	0.293	0.541	26.103	0.359	0.120	0.311	0.342	0.178	0.305	0.109	0.722	0.265	0.240	
0.3	0.35	137.012	0.736	0.922	2.973	0.458	0.731	30.134	0.376	0.127	0.391	0.391	0.194	0.293	0.152	1.065	0.392	0.346	
0.3	0.4	142.497	1.019	1.244	38.787	0.443	0.987	15.002	0.457	0.130	0.462	0.448	0.262	0.259	0.160	1.775	1.110	1.005	
0.3	0.45	141.926	1.359	1.445	5.162	0.530	1.165	16.997	0.504	0.137	0.508	0.501	0.307	0.239	0.181	2.159	1.170	1.055	
0.35	0.35	114.803	0.741	0.818	27.088	0.415	0.648	41.743	0.391	0.143	0.360	0.396	0.172	0.411	0.106	1.034	0.365	0.285	
0.35	0.4	118.403	1.053	1.180	63.018	0.449	0.911	30.182	0.468	0.149	0.460	0.452	0.230	0.377	0.132	0.981	0.402	0.309	
0.35	0.45	118.157	1.416	1.446	28.210	0.540	1.174	32.558	0.498	0.156	0.515	0.505	0.301	0.311	0.172	1.500	0.819	0.629	
0.4	0.4	96.566	1.047	1.093	53.206	0.478	0.823	52.636	0.450	0.169	0.391	0.456	0.205	0.417	0.168	0.945	0.335	0.223	
0.4	0.45	101.591	1.456	1.405	37.268	0.545	1.082	59.120	0.486	0.175	0.519	0.509	0.258	0.416	0.166	1.071	0.311	0.203	
0.45	0.45	86.252	1.466	1.292	11.308	0.624	1.037	61.555	0.532	0.195	0.449	0.514	0.291	0.415	0.186	0.787	0.383	0.179	
Helium – Helium/Carbon/Oxygen																			
0.2	0.5	228.886	1.739	1.641	1.613	0.541	1.296	2.115	0.541	0.109	0.531	0.540	0.405	0.155	0.093	4.474	2.025	2.243	
0.2	0.55	229.339	2.289	1.993	39.066	0.555	1.416	46.742	0.557	0.111	0.577	0.593	0.402	0.208	0.092	4.477	2.732	2.846	
0.2	0.6	230.037	3.008	2.072	59.437	0.602	1.673	27.744	0.614	0.116	0.619	0.645	0.473	0.188	0.091	4.488	3.457	3.312	
0.25	0.5	177.730	1.766	1.866	14.913	0.539	1.395	6.520	0.547	0.126	0.539	0.548	0.378	0.209	0.134	2.697	2.511	2.539	
0.25	0.55	178.772	2.310	1.937	4.978	0.600	1.528	3.145	0.606	0.134	0.587	0.597	0.425	0.208	0.128	3.596	2.523	2.491	
0.25	0.6	179.892	3.002	2.364	61.484	0.614	1.688	69.397	0.606	0.136	0.635	0.654	0.477	0.208	0.130	3.234	3.044	2.792	
0.3	0.5	143.922	1.814	1.882	34.897	0.523	1.395	23.735	0.538	0.143	0.556	0.554	0.374	0.234	0.169	2.105	1.738	1.548	
0.3	0.55	146.260	2.335	2.206	10.328	0.614	1.613	8.333	0.614	0.150	0.595	0.607	0.413	0.238	0.163	3.408	2.335	2.017	
0.3	0.6	146.020	3.054	2.401	130.200	0.593	1.814	6.262	0.662	0.159	0.645	0.657	0.448	0.256	0.164	2.915	2.832	2.356	
0.35	0.5	120.603	1.874	1.959	28.288	0.560	1.468	24.337	0.565	0.162	0.565	0.560	0.351	0.285	0.194	1.889	1.394	1.069	
0.35	0.55	121.539	2.414	2.236	40.264	0.602	1.659	22.942	0.612	0.170	0.602	0.612	0.395	0.286	0.197	2.067	1.242	0.972	
0.35	0.6	120.954	3.114	2.573	51.150	0.635	1.861	51.150	0.635	0.179	0.654	0.661	0.445	0.259	0.219	2.503	2.123	1.586	
0.4	0.5	102.523	1.922	2.012	132.652	0.509	1.456	62.742	0.554	0.184	0.577	0.561	0.323	0.366	0.200	1.079	0.738	0.495	
0.4	0.55	103.503	2.488	2.331	44.860	0.618	1.697	23.024	0.640	0.189	0.628	0.618	0.372	0.335	0.228	1.309	1.068	0.712	
0.4	0.6	103.109	3.195	2.644	43.660	0.664	1.915	44.352	0.664	0.196	0.663	0.669	0.407	0.357	0.214	2.011	1.447	0.975	
0.45	0.5	88.221	2.008	1.915	105.100	0.554	1.373	117.948	0.528	0.202	0.576	0.565	0.291	0.477	0.174	0.707	0.609	0.311	
0.45	0.55	88.850	2.592	2.354	54.571	0.626	1.724	73.256	0.594	0.210	0.639	0.622	0.343	0.430	0.215	1.144	0.875	0.421	
0.45	0.6	89.581	3.303	2.694	26.982	0.693	1.975	72.952	0.654	0.218	0.685	0.674	0.391	0.391	0.247	1.927	1.252	0.662	
Helium/Carbon/Oxygen – Helium/Carbon/Oxygen																			
0.5	0.5	74.362	2.029	2.170	174.519	0.503	1.760	88.536	0.563	0.216	0.544	0.576	0.261	0.567	0.165	0.596	0.624	0.120	
0.5	0.55	75.401	2.701	2.622	243.511	0.566	2.131	192.096	0.584	0.224	0.644	0.633	0.342	0.473	0.224	1.048	0.970	0.214	
0.5	0.6	74.288	3.438	3.133	155.623	0.663	2.467	108.393	0.649	0.235	0.678	0.673	0.362	0.471	0.248	1.639	1.978	0.415	
0.55	0.55	66.277	2.755	3.087	200.887	0.571	2.569	90.632	0.661	0.232	0.632	0.632	0.310	0.568	0.210	0.981	2.807	0.351	
0.55	0.6	66.680	3.456	4.032	90.061	0.647	3.281	84.085	0.663	0.229	0.672	0.682	0.375	0.521	0.228	2.002	6.341	0.575	
0.6	0.6	59.194	3.370	4.179	102.862	0.642	3.552	102.862	0.642	0.235	0.647	0.679	0.329	0.456	0.379	2.352	12.681	1.007	

Continued on next page...

Table A1 – Continued

$M_{\rm don}$ $M_\odot$	$M_{\rm acc}$ $M_\odot$	P_0 s	$\rho_{\rm max}$ 10^6 g/cm^3	$T_{\rm max}$ 10^8 K	$\rho(T_{\rm max})$ 10^3 g/cm^3	$M(T_{\rm max})$ $M_\odot$	$\langle T\rangle_{\rm max}$ 10^8 K	$\rho(\langle T\rangle_{\rm max})$ 10^3 g/cm^3	$M(\langle T\rangle_{\rm max})$ $M_\odot$	$\omega_{\rm max}$ rad/s	$M(\omega_{\rm max})$ $M_\odot$	$M(\omega_{\rm k}/2)$ $M_\odot$	$M_{\rm core}$ $M_\odot$	$M_{\rm env}$ $M_\odot$	$M_{\rm disk}$ $M_\odot$	$M_{\rm fb}$ $10^{-2}M_\odot$	$M_{\rm esc}$ $10^{-3}M_\odot$	$L_{\rm esc}$ $\%L_{\rm tot}$	Outcome
Helium – Carbon/Oxygen																			
0.2	0.65	230.434	3.911	2.740	52.593	0.654	1.982	28.511	0.663	0.120	0.673	0.692	0.504	0.206	0.102	3.301	4.022	3.731	
0.2	0.7	229.756	5.097	2.841	54.098	0.706	2.277	31.882	0.711	0.126	0.477	0.742	0.567	0.191	0.100	3.750	5.090	4.331	
0.2	0.75	232.641	6.568	3.052	36.193	0.760	2.562	30.778	0.768	0.131	0.750	0.792	0.594	0.212	0.084	5.399	6.394	5.231	
0.2	0.8	231.157	8.586	3.976	31.743	0.806	3.262	24.823	0.812	0.135	0.795	0.841	0.664	0.191	0.100	3.708	7.794	5.969	
0.2	0.85	235.614							does not merge after 86 × P_0										
0.2	0.9	235.165	14.003	4.899	19.740	0.907	4.291	14.474	0.914	0.142	0.062	0.939	0.730	0.222	0.083	5.272	11.732	8.152	
0.2	0.95	235.215	16.594	4.847	20.894	0.954	4.310	15.272	0.959	0.150	0.051	0.989	0.704	0.298	0.057	7.357	17.446	12.408	
0.2	1	234.578	21.742	5.264	22.916	1.002	4.534	12.925	1.008	0.159	0.998	1.033	0.762	0.280	0.088	5.356	16.031	10.387	
0.2	1.05	235.761							does not merge after 77.5 × P_0										
0.25	0.65	180.932	3.923	2.744	63.787	0.664	2.075	81.452	0.645	0.144	0.668	0.703	0.507	0.223	0.126	4.011	3.042	2.584	
0.25	0.7	181.024	5.102	3.164	70.063	0.711	2.292	54.088	0.717	0.151	0.153	0.754	0.554	0.218	0.121	5.268	3.650	2.878	
0.25	0.75	182.846	6.583	3.755	70.664	0.759	2.561	45.251	0.770	0.157	0.776	0.803	0.617	0.206	0.118	5.464	4.714	3.556	
0.25	0.8	182.183	8.434	4.463	38.723	0.804	3.737	31.002	0.816	0.160	0.090	0.852	0.654	0.215	0.121	5.437	5.825	4.141	
0.25	0.85	184.417	10.538	4.875	21.456	0.858	4.340	19.115	0.864	0.161	0.856	0.902	0.677	0.244	0.123	4.888	7.221	5.026	
0.25	0.9	183.236	13.566	5.224	21.967	0.902	4.582	16.745	0.908	0.181	0.901	0.948	0.740	0.222	0.117	6.258	8.297	5.344	
0.25	0.95	184.034	17.224	5.105	19.319	0.956	4.685	15.256	0.961	0.188	0.952	0.992	0.780	0.228	0.091	8.646	15.365	9.193	
0.25	1	184.290	23.082	5.583	28.908	1.001	4.983	13.359	1.010	0.211	1.004	1.038	0.823	0.224	0.127	6.373	13.183	7.536	
0.25	1.05	185.003	29.167	5.657	23.106	1.052	5.025	15.149	1.059	0.204	1.050	1.088	0.827	0.279	0.121	5.975	13.900	8.159	
0.3	0.65	146.813	3.964	2.752	9.190	0.711	2.232	105.983	0.641	0.171	0.689	0.708	0.497	0.248	0.154	4.749	2.874	2.339	
0.3	0.7	146.585	5.113	3.242	149.740	0.688	2.508	156.919	0.680	0.173	0.742	0.762	0.581	0.214	0.167	3.544	3.177	2.465	
0.3	0.75	147.840	6.603	3.621	82.347	0.773	2.745	173.410	0.738	0.182	0.790	0.811	0.595	0.247	0.142	6.191	3.974	2.876	
0.3	0.8	147.050	8.275	4.739	68.888	0.807	3.661	50.374	0.816	0.183	0.790	0.861	0.649	0.241	0.147	5.848	4.651	3.107	
0.3	0.85	149.691	10.368	5.188	42.981	0.856	4.523	23.206	0.865	0.188	0.002	0.911	0.707	0.228	0.160	4.918	5.105	3.233	
0.3	0.9	149.108	13.171	5.279	25.217	0.906	4.678	20.180	0.910	0.192	0.904	0.957	0.754	0.223	0.154	6.127	8.004	4.747	
0.3	0.95	149.422	16.915	5.475	29.697	0.953	4.814	17.958	0.961	0.206	0.950	1.000	0.767	0.250	0.146	7.545	12.391	6.690	
0.3	1	149.953	22.586	5.629	31.051	1.002	5.141	14.832	1.011	0.227	1.000	1.048	0.790	0.271	0.133	9.516	10.832	5.708	
0.3	1.05	150.690	30.706	5.864	34.484	1.051	5.382	14.531	1.059	0.265	1.051	1.091	0.885	0.223	0.148	8.043	12.919	6.469	
0.35	0.65	121.642	4.045	2.978	37.689	0.701	2.349	135.768	0.639	0.187	0.705	0.716	0.490	0.274	0.200	3.377	2.668	1.972	
0.35	0.7	122.430	5.156	3.224	137.712	0.715	2.549	155.470	0.690	0.199	0.745	0.764	0.524	0.282	0.201	3.977	2.909	2.060	
0.35	0.75	123.539	6.592	3.685	17.646	0.816	2.842	239.128	0.717	0.210	0.798	0.813	0.584	0.276	0.208	2.981	3.123	2.175	
0.35	0.8	122.852	8.287	4.978	107.360	0.806	3.699	96.419	0.811	0.202	0.803	0.866	0.651	0.254	0.200	4.170	3.490	2.279	
0.35	0.85	124.890	10.152	5.715	63.928	0.854	4.599	26.507	0.869	0.219	0.854	0.920	0.676	0.287	0.188	4.502	3.675	2.235	
0.35	0.9	125.082	12.975	5.884	57.009	0.902	4.775	20.711	0.917	0.219	0.900	0.962	0.720	0.268	0.212	4.531	4.608	2.669	
0.35	0.95	124.644	16.407	5.777	52.520	0.951	4.751	19.982	0.963	0.226	0.951	1.009	0.773	0.250	0.210	5.624	11.037	5.493	
0.35	1	125.596	22.122	6.101	38.868	1.002	5.029	23.317	1.006	0.255	1.000	1.055	0.793	0.277	0.211	6.042	8.292	4.218	
0.35	1.05	125.409	29.235	6.784	63.511	1.049	5.195	16.471	1.060	0.271	1.050	1.101	0.869	0.250	0.208	6.154	11.052	5.166	
0.4	0.65	103.817	4.141	3.212	43.898	0.713	2.397	185.441	0.630	0.207	0.724	0.721	0.462	0.337	0.224	2.466	2.108	1.407	
0.4	0.7	104.815	5.288	3.375	16.512	0.786	2.720	179.546	0.690	0.216	0.765	0.775	0.519	0.324	0.226	2.853	2.667	1.729	
0.4	0.75	104.650	6.735	3.847	25.780	0.824	2.988	258.232	0.722	0.226	0.788	0.822	0.562	0.311	0.239	3.396	3.018	1.923	
0.4	0.8	105.005	8.549	5.148	193.044	0.800	3.447	218.119	0.797	0.238	0.844	0.866	0.620	0.296	0.240	4.003	3.380	2.077	
0.4	0.85	105.398	10.219	5.896	40.741	0.863	4.679	33.674	0.870	0.245	0.853	0.921	0.673	0.296	0.233	4.328	4.447	2.562	
0.4	0.9	105.854	12.432	5.773	32.572	0.911	4.863	25.181	0.913	0.234	0.897	0.974	0.688	0.288	0.271	4.819	5.293	2.627	
0.4	0.95	106.466	15.976	6.448	70.841	0.948	4.885	21.718	0.965	0.247	0.947	1.017	0.729	0.307	0.249	5.651	7.975	3.454	
0.4	1	106.900	21.120	6.064	43.036	1.000	5.102	16.958	1.013	0.272	0.997	1.059	0.806	0.282	0.250	5.202	10.570	4.438	
0.4	1.05	107.339	28.328	6.518	39.046	1.050	5.399	19.819	1.057	0.281	1.048	1.106	0.897	0.221	0.257	6.527	10.118	4.287	
0.45	0.65	89.708	4.234	3.324	52.587	0.734	2.436	83.398	0.698	0.226	0.720	0.727	0.444	0.359	0.267	2.931	1.181	0.693	
0.45	0.7	89.157	5.402	3.584	166.312	0.711	2.751	188.196	0.696	0.237	0.765	0.778	0.500	0.350	0.278	2.075	1.495	0.852	
0.45	0.75	90.732	6.833	4.244	68.312	0.814	3.078	209.468	0.739	0.248	0.808	0.828	0.566	0.336	0.268	2.676	2.326	1.286	
0.45	0.8	90.876	8.145	6.011	85.187	0.815	4.227	84.626	0.817	0.246	0.807	0.882	0.620	0.313	0.272	4.163	2.900	1.468	
0.45	0.85	89.934	9.635	5.683	73.832	0.844	4.636	37.089	0.865	0.245	0.850	0.933	0.659	0.301	0.284	5.059	6.086	2.345	
0.45	0.9	91.636	11.785	6.186	56.092	0.901	4.983	38.794	0.901	0.256	0.893	0.968	0.689	0.310	0.284	5.866	8.509	2.918	
0.45	0.95	91.470	15.542	6.476	90.665	0.942	5.138	22.826	0.959	0.279	0.943	0.997	0.759	0.261	0.291	7.608	12.992	4.139	
0.45	1	92.022	20.037	6.343	35.357	0.995	5.113	36.875	0.993	0.278	0.991	1.052	0.789	0.279	0.291	7.303	17.651	5.735	

Continued on next page...

Table A1 – Continued

$M_{\rm don}$ $M_\odot$	$M_{\rm acc}$ $M_\odot$	P_0 s	$\rho_{\rm max}$ 10^6 g/cm^3	$T_{\rm max}$ 10^8 K	$\rho(T_{\rm max})$ 10^3 g/cm^3	$M(T_{\rm max})$ $M_\odot$	$\langle T\rangle_{\rm max}$ 10^8 K	$\rho(\langle T\rangle_{\rm max})$ 10^3 g/cm^3	$M(\langle T\rangle_{\rm max})$ $M_\odot$	$\omega_{\rm max}$ rad/s	$M(\omega_{\rm max})$ $M_\odot$	$M(\omega_{\rm k}/2)$ $M_\odot$	$M_{\rm core}$ $M_\odot$	$M_{\rm env}$ $M_\odot$	$M_{\rm disk}$ $M_\odot$	$M_{\rm fb}$ $10^{-2}M_\odot$	$M_{\rm esc}$ $10^{-3}M_\odot$	$L_{\rm esc}$ $\%L_{\rm tot}$	Outcome
0.45	1.05	92.531	27.016	6.746	83.393	1.040	5.306	87.909	1.039	0.290	1.043	1.101	0.828	0.282	0.308	6.621	16.294	5.717	
Helium/Carbon/Oxygen – Carbon/Oxygen																			
0.5	0.65	77.846	4.385	3.477	57.549	0.746	2.810	78.616	0.716	0.246	0.742	0.733	0.434	0.423	0.272	1.927	1.748	0.522	
0.5	0.7	77.677	5.563	3.857	33.316	0.794	3.172	95.099	0.760	0.258	0.776	0.780	0.562	0.367	0.290	-2.036	2.544	0.736	
0.5	0.75	77.792	6.995	4.153	90.687	0.798	3.412	144.790	0.776	0.269	0.817	0.834	0.544	0.392	0.282	2.927	2.913	0.796	
0.5	0.8	78.410	8.859	4.667	45.821	0.871	3.760	222.249	0.812	0.277	0.862	0.880	0.592	0.391	0.275	3.694	5.393	1.413	
0.5	0.85	78.621	11.127	8.869	14.421	1.023	4.141	418.228	0.843	0.289	0.903	0.927	0.653	0.342	0.306	4.057	9.329	2.294	
0.5	0.9	79.102	14.166	5.482	54.356	0.967	4.584	326.166	0.888	0.303	0.944	0.971	0.678	0.367	0.302	4.275	9.991	2.324	
0.5	0.95	79.346	18.514	6.015	583.849	0.920	5.128	408.402	0.953	0.323	1.001	1.025	0.739	0.356	0.299	4.602	9.638	2.809	
0.5	1	80.422	24.354	6.635	332.741	0.998	5.611	488.456	0.985	0.346	1.050	1.071	0.764	0.375	0.291	5.641	13.235	4.050	
0.5	1.05	80.310	32.680	7.113	464.021	1.046	6.228	617.862	1.034	0.370	1.100	1.119	0.842	0.327	0.305	6.354	12.928	4.309	
0.55	0.65	67.241	4.446	4.006	416.649	0.620	3.239	90.766	0.713	0.254	0.723	0.738	0.396	0.516	0.265	1.817	4.477	0.526	
0.55	0.7	68.252	5.642	4.304	67.964	0.772	3.501	97.451	0.754	0.265	0.772	0.785	0.479	0.449	0.285	3.060	6.665	0.852	
0.55	0.75	68.037	6.987	4.693	52.523	0.820	3.763	96.541	0.790	0.274	0.816	0.827	0.508	0.431	0.311	3.880	10.624	1.230	
0.55	0.8	69.026	8.705	5.169	55.063	0.864	4.064	127.112	0.837	0.288	0.859	0.873	0.557	0.411	0.325	4.200	14.302	1.796	
0.55	0.85	69.081	10.995	5.292	34.265	0.929	4.297	216.763	0.855	0.306	0.917	0.920	0.632	0.367	0.339	4.545	15.845	2.165	
0.55	0.9	69.554	13.928	6.329	92.468	0.978	4.741	328.682	0.884	0.321	0.958	0.969	0.653	0.385	0.340	5.509	17.503	2.585	
0.55	0.95	70.081	18.147	5.970	789.231	0.896	5.138	314.783	0.944	0.338	0.986	1.021	0.717	0.406	0.308	4.840	20.830	4.124	
0.55	1	70.446	24.158	9.787	244.069	1.033	5.665	459.437	0.989	0.366	1.042	1.065	0.760	0.373	0.329	6.691	20.797	4.830	
0.55	1.05	70.093	32.859	7.175	753.509	1.024	6.423	458.041	1.055	0.385	1.091	1.124	0.849	0.323	0.346	6.275	19.470	4.918	
0.6	0.65	59.832	4.514	4.597	144.793	0.729	3.806	97.853	0.712	0.262	0.723	0.733	0.421	0.428	0.369	2.240	8.959	0.686	
0.6	0.7	60.050	5.645	4.977	78.272	0.786	4.238	86.751	0.758	0.264	0.743	0.794	0.444	0.504	0.306	3.348	13.588	1.088	
0.6	0.75	59.984	6.863	9.048	62.639	0.913	4.291	98.371	0.816	0.282	0.799	0.829	0.466	0.475	0.349	4.224	18.269	1.408	
0.6	0.8	60.960	8.734	5.371	64.380	0.884	4.408	163.915	0.815	0.293	0.854	0.877	0.535	0.428	0.364	4.862	24.721	2.227	
0.6	0.85	61.237	10.809	5.484	66.283	0.916	4.537	71.821	0.923	0.312	0.909	0.920	0.602	0.427	0.334	5.929	27.764	2.487	
0.6	0.9	61.262	13.922	5.840	160.281	0.929	4.911	331.915	0.898	0.333	0.952	0.969	0.648	0.411	0.367	4.583	28.932	2.686	
0.6	0.95	62.184	18.030	6.256	63.335	1.010	5.274	355.850	0.940	0.354	0.986	1.019	0.715	0.388	0.359	5.781	30.384	4.233	
0.6	1	62.202	23.732	6.932	88.429	1.050	5.884	496.703	0.972	0.381	1.040	1.074	0.790	0.359	0.365	5.594	30.669	5.051	
0.6	1.05	62.032	31.703	7.333	768.514	1.014	6.524	596.270	1.029	0.407	1.079	1.120	0.805	0.390	0.364	5.652	34.037	6.606	
Carbon/Oxygen – Carbon/Oxygen																			
0.65	0.65	51.865	4.498	3.229	700.736	0.559	2.704	218.810	0.703	0.333	0.599	0.738	0.289	0.797	0.200	1.319	0.205	0.080	
0.65	0.7	53.239	5.990	3.977	172.768	0.802	3.192	268.065	0.742	0.343	0.802	0.787	0.382	0.734	0.220	1.415	0.178	0.063	
0.65	0.75	53.749	7.712	4.591	666.019	0.753	3.750	217.223	0.838	0.358	0.864	0.838	0.468	0.601	0.311	2.004	0.354	0.143	
0.65	0.8	54.470	9.814	5.063	308.348	0.848	4.254	200.931	0.892	0.375	0.891	0.891	0.516	0.540	0.373	2.014	0.538	0.217	
0.65	0.85	54.133	12.626	5.482	191.333	0.915	4.660	225.467	0.915	0.391	0.948	0.948	0.573	0.519	0.384	2.312	1.002	0.414	
0.65	0.9	53.986	16.218	6.065	145.986	0.994	5.136	163.126	0.976	0.411	1.003	0.999	0.637	0.489	0.393	2.975	1.025	0.436	
0.65	0.95	54.432	21.360	6.552	221.599	1.027	5.477	195.902	1.022	0.434	1.040	1.048	0.705	0.463	0.395	3.581	1.252	0.527	
0.65	1	54.640	28.183	6.902	361.440	1.068	6.083	358.800	1.040	0.459	1.096	1.103	0.746	0.457	0.406	3.966	1.388	0.556	
0.65	1.05	55.136	38.207	7.707	1381.898	1.027	6.809	988.864	1.027	0.489	1.131	1.163	0.823	0.438	0.397	3.947	2.110	0.823	
0.7	0.7	46.842	5.796	3.732	771.280	0.655	3.064	234.975	0.792	0.374	0.666	0.792	0.340	0.813	0.231	1.582	0.109	0.038	
0.7	0.75	48.161	7.817	4.665	681.538	0.808	3.640	267.291	0.824	0.384	0.832	0.840	0.408	0.760	0.264	1.830	0.110	0.037	
0.7	0.8	47.824	10.220	5.438	913.532	0.788	4.253	311.627	0.844	0.410	0.900	0.887	0.481	0.687	0.309	2.277	0.193	0.072	
0.7	0.85	48.301	13.021	5.912	397.345	0.943	4.735	203.383	0.943	0.428	0.973	0.949	0.533	0.607	0.384	2.515	0.578	0.223	
0.7	0.9	48.243	16.723	6.313	276.838	0.990	5.244	166.696	1.012	0.449	1.017	0.995	0.593	0.579	0.399	2.772	0.922	0.351	
0.7	0.95	48.480	21.914	6.866	373.104	1.023	5.814	188.279	1.059	0.471	1.044	1.054	0.658	0.539	0.420	3.269	1.016	0.404	
0.7	1	84.987	29.338	7.173	787.639	1.028	6.374	1064.668	0.976	0.492	0.359	1.141	0.731	0.527	0.415	2.570	1.085	0.427	
0.7	1.05	48.875	38.881	8.005	792.237	1.058	6.868	186.278	1.155	0.532	1.135	1.155	0.798	0.456	0.456	3.769	1.778	0.674	
0.75	0.75	42.406	7.664	4.654	1111.741	0.669	3.536	477.711	0.785	0.420	0.753	0.854	0.346	0.883	0.263	0.759	0.231	0.074	
0.75	0.8	47.046	10.249	5.175	1084.536	0.812	4.158	423.421	0.840	0.434	0.866	0.900	0.443	0.797	0.293	1.660	0.166	0.052	
0.75	0.85	42.771	13.332	5.689	1100.392	0.851	4.751	499.338	0.901	0.459	0.970	0.948	0.525	0.696	0.363	1.508	0.121	0.045	
0.75	0.9	43.153	17.344	6.656	232.610	1.007	5.496	286.758	1.001	0.482	1.001	1.001	0.575	0.643	0.412	1.892	0.694	0.222	
0.75	0.95	43.452	22.299	7.037	250.783	1.089	5.886	351.801	1.029	0.507	1.072	1.054	0.637	0.584	0.455	2.202	0.884	0.312	

Continued on next page...

Table A1 – Continued

$M_{\rm don}$ $M_\odot$	$M_{\rm acc}$ $M_\odot$	P_0 s	$\rho_{\rm max}$ 10^6 g/cm^3	$T_{\rm max}$ 10^8 K	$\rho(T_{\rm max})$ 10^3 g/cm^3	$M(T_{\rm max})$ $M_\odot$	$\langle T\rangle_{\rm max}$ 10^8 K	$\rho(\langle T\rangle_{\rm max})$ 10^3 g/cm^3	$M(\langle T\rangle_{\rm max})$ $M_\odot$	$\omega_{\rm max}$ rad/s	$M(\omega_{\rm max})$ $M_\odot$	$M(\omega_{\rm k}/2)$ $M_\odot$	$M_{\rm core}$ $M_\odot$	$M_{\rm env}$ $M_\odot$	$M_{\rm disk}$ $M_\odot$	$M_{\rm fb}$ $10^{-2}M_\odot$	$M_{\rm esc}$ $10^{-3}M_\odot$	$L_{\rm esc}$ $\%L_{\rm tot}$	Outcome
0.75	1	43.607	29.622	7.598	208.763	1.101	6.463	683.181	1.034	0.539	1.095	1.105	0.733	0.536	0.452	2.792	0.864	0.308	
0.75	1.05	44.025	39.943	8.285	382.368	1.152	7.157	446.014	1.104	0.572	1.137	1.161	0.777	0.511	0.476	3.516	1.174	0.420	
0.8	0.8	38.085	10.045	4.978	1597.373	0.747	4.101	963.585	0.770	0.472	0.725	0.919	0.375	0.920	0.294	1.108	0.108	0.031	
0.8	0.85	38.448	13.646	5.933	943.778	0.902	4.905	392.917	0.929	0.490	0.901	0.956	0.455	0.853	0.326	1.571	0.170	0.044	
0.8	0.9	38.854	17.806	6.540	1168.151	0.901	5.500	561.438	0.953	0.521	0.994	1.002	0.562	0.705	0.405	2.751	0.196	0.058	
0.8	0.95	38.854	23.346	7.706	586.806	1.007	6.031	338.403	1.042	0.550	1.078	1.057	0.617	0.644	0.467	2.070	0.641	0.191	
0.8	1	39.187	30.463	7.842	690.128	1.078	6.717	563.213	1.051	0.581	1.117	1.110	0.693	0.636	0.440	3.050	0.630	0.213	
0.8	1.05	39.058	41.284	8.694	1160.689	1.105	7.404	370.513	1.148	0.616	1.148	1.165	0.766	0.559	0.492	3.059	1.147	0.377	
0.85	0.85	33.992	13.196	6.076	1670.837	0.772	4.635	576.422	0.951	0.533	0.817	0.972	0.392	0.954	0.343	1.100	0.099	0.026	
0.85	0.9	34.660	18.203	6.961	1045.649	0.959	5.581	760.399	0.959	0.553	1.006	1.006	0.487	0.827	0.417	1.749	0.358	0.082	
0.85	0.95	34.501	24.142	7.599	1779.133	0.912	6.293	809.584	1.030	0.589	1.062	1.054	0.572	0.788	0.414	2.651	0.349	0.081	
0.85	1	34.727	31.535	8.395	1450.772	1.056	6.967	720.451	1.065	0.625	1.117	1.110	0.653	0.689	0.483	2.437	0.561	0.139	
0.85	1.05	34.826	42.932	9.071	724.831	1.135	7.671	814.835	1.091	0.668	1.167	1.161	0.702	0.677	0.486	3.387	0.723	0.204	
0.9	0.9	30.310	17.425	6.352	2669.223	0.805	5.376	841.261	0.950	0.601	0.853	1.017	0.449	1.046	0.293	1.267	0.342	0.071	
0.9	0.95	31.222	24.741	8.271	2358.052	0.899	6.480	1102.244	1.011	0.628	1.058	1.068	0.551	0.889	0.392	1.741	0.240	0.046	
0.9	1	31.100	32.846	8.560	1609.054	0.991	7.291	1207.070	1.066	0.674	1.108	1.108	0.636	0.770	0.472	2.200	0.262	0.053	
0.9	1.05	31.184	44.074	9.554	3248.604	0.980	7.868	553.130	1.148	0.718	1.155	1.163	0.679	0.757	0.488	2.546	0.766	0.164	
0.95	0.95	27.414	23.920	7.315	3748.350	0.800	6.153	1069.803	0.984	0.672	0.948	1.077	0.472	1.042	0.369	1.628	0.366	0.068	
0.95	1	27.583	34.590	9.961	2591.980	0.970	7.262	1114.504	1.054	0.713	1.102	1.121	0.605	0.881	0.447	1.646	0.562	0.091	
0.95	1.05	27.714	46.075	10.191	1668.466	1.130	8.219	961.232	1.157	0.766	1.157	1.174	0.640	0.829	0.510	1.982	0.627	0.103	
1	1	24.311	31.069	9.165	1899.998	1.059	7.012	1415.971	1.035	0.765	0.972	1.119	0.484	1.078	0.422	1.514	0.764	0.104	
1	1.05	24.931	48.777	10.758	2942.135	1.090	8.512	2329.601	1.070	0.819	1.160	1.180	0.600	0.961	0.470	1.780	0.850	0.119	
1.05	1.05	21.361	46.198	10.407	3413.441	1.106	8.620	4231.055	0.994	0.871	1.081	1.176	0.513	1.020	0.547	1.795	1.453	0.125	
Helium – Oxygen/Neon																			
0.2	1.1	236.693	does not merge after 84 × P_0																
0.2	1.15	238.214	does not merge after 80 × P_0																
0.2	1.2	235.168	does not merge after 80 × P_0																
0.25	1.1	186.210	does not merge after 75 × P_0																
0.25	1.15	185.373	does not merge after 75 × P_0																
0.25	1.2	185.471	does not merge after 80 × P_0																
0.3	1.1	151.295	40.873	6.449	28.069	1.103	5.525	12.290	1.110	0.261	1.100	1.138	0.907	0.238	0.142	9.562	16.247	7.654	
0.3	1.15	150.134	57.305	6.384	117.765	1.149	5.704	17.799	1.154	0.320	1.150	1.185	0.930	0.265	0.138	9.668	19.818	8.831	
0.3	1.2	151.476	79.510	7.318	48.858	1.204	5.780	20.762	1.208	0.296	1.205	1.232	0.952	0.289	0.151	8.617	21.295	9.421	
0.35	1.1	124.643	38.839	6.798	49.035	1.100	5.630	17.097	1.107	0.282	1.099	1.144	0.900	0.256	0.206	7.158	16.222	7.540	
0.35	1.15	125.184	50.143	7.904	73.854	1.151	5.963	980.481	1.087	0.281	1.155	1.193	0.880	0.326	0.204	6.730	22.376	10.792	
0.35	1.2	126.520	81.018	7.674	44.376	1.200	6.140	25.883	1.205	0.342	1.200	1.234	0.964	0.279	0.197	8.837	21.441	7.998	
0.4	1.1	106.581	39.735	7.046	54.698	1.098	5.815	23.236	1.108	0.301	1.099	1.145	0.905	0.249	0.265	6.815	12.563	5.051	
0.4	1.15	107.435	53.919	7.486	60.355	1.148	5.927	22.787	1.154	0.340	1.149	1.191	0.933	0.262	0.254	8.498	16.053	6.120	
0.4	1.2	107.690	81.457	7.631	1043.333	1.151	6.595	1346.704	1.132	0.376	1.198	1.234	0.994	0.244	0.257	8.702	18.754	6.514	
0.45	1.1	91.509	37.159	7.328	72.652	1.095	5.669	120.311	1.091	0.320	1.095	1.146	0.921	0.249	0.277	8.683	16.421	5.736	
0.45	1.15	91.732	53.949	7.848	173.361	1.140	6.033	36.254	1.150	0.338	1.147	1.191	0.937	0.278	0.291	7.885	15.283	5.139	
0.45	1.2	92.617	78.080	8.501	49.249	1.196	6.572	18.771	1.205	0.395	1.196	1.235	0.970	0.280	0.303	7.640	20.070	6.293	
Helium/Carbon/Oxygen – Oxygen/Neon																			
0.5	1.1	79.774	46.507	8.512	627.041	1.092	7.254	553.186	1.096	0.394	1.152	1.173	0.881	0.337	0.304	6.701	11.159	3.767	
0.5	1.15	80.598	64.642	9.044	607.305	1.147	7.964	554.041	1.150	0.431	1.185	1.219	0.947	0.310	0.320	6.055	12.617	4.445	
0.5	1.2	81.316	96.250	10.487	876.008	1.188	8.932	469.217	1.219	0.472	1.235	1.266	0.982	0.322	0.310	7.206	13.220	4.189	
0.55	1.1	70.267	46.091	8.637	770.185	1.078	7.163	569.397	1.096	0.421	1.141	1.171	0.905	0.327	0.339	6.111	17.319	4.800	
0.55	1.15	70.343	64.596	9.583	857.534	1.141	8.175	1092.033	1.128	0.465	1.197	1.221	0.976	0.302	0.337	7.014	15.330	4.488	
0.55	1.2	71.280	96.559	10.874	1132.422	1.183	9.215	738.608	1.203	0.503	1.242	1.272	0.990	0.322	0.357	6.541	15.508	4.462	
0.6	1.1	62.111	45.826	8.548	928.747	1.075	7.539	729.351	1.080	0.445	1.160	1.176	0.914	0.319	0.382	6.138	23.325	4.832	
0.6	1.15	62.454	63.549	9.473	1705.963	1.095	8.310	895.597	1.135	0.486	1.196	1.226	0.939	0.346	0.377	6.511	22.944	5.373	
0.6	1.2	62.510	95.710	10.631	855.484	1.201	9.446	1109.502	1.184	0.538	1.231	1.274	1.016	0.316	0.381	6.772	19.251	4.645	

Continued on next page...

Table A1 – Continued

$M_{\rm don}$ $M_\odot$	$M_{\rm acc}$ $M_\odot$	P_0 s	$\rho_{\rm max}$ 10^6 g/cm^3	$T_{\rm max}$ 10^8 K	$\rho(T_{\rm max})$ 10^3 g/cm^3	$M(T_{\rm max})$ $M_\odot$	$\langle T\rangle_{\rm max}$ 10^8 K	$\rho(\langle T\rangle_{\rm max})$ 10^3 g/cm^3	$M(\langle T\rangle_{\rm max})$ $M_\odot$	$\omega_{\rm max}$ rad/s	$M(\omega_{\rm max})$ $M_\odot$	$M(\omega_{\rm k}/2)$ $M_\odot$	$M_{\rm core}$ $M_\odot$	$M_{\rm env}$ $M_\odot$	$M_{\rm disk}$ $M_\odot$	$M_{\rm fb}$ $10^{-2}M_\odot$	$M_{\rm esc}$ $10^{-3}M_\odot$	$L_{\rm esc}$ $\%L_{\rm tot}$	Outcome
Carbon/Oxygen – Oxygen/Neon																			
0.65	1.1	55.281	52.503	8.736	1317.569	1.088	7.706	872.186	1.115	0.525	1.179	1.206	0.852	0.434	0.405	5.581	3.180	1.194	
0.65	1.15	55.270	73.902	9.801	1060.712	1.166	8.564	1518.323	1.140	0.578	1.224	1.249	0.933	0.388	0.409	6.573	3.644	1.324	
0.65	1.2	53.732	112.982	11.610	1602.232	1.188	10.346	1806.667	1.194	0.635	1.251	1.306	0.975	0.398	0.417	5.627	4.258	1.384	
0.7	1.1	49.191	54.180	9.459	1388.710	1.102	7.784	1137.366	1.095	0.569	1.181	1.210	0.889	0.401	0.465	4.367	1.995	0.726	
0.7	1.15	49.330	75.394	10.036	1282.083	1.159	8.765	1195.404	1.143	0.623	1.214	1.251	0.907	0.423	0.461	5.630	2.312	0.804	
0.7	1.2	49.286	113.915	11.315	1217.284	1.232	10.081	1590.375	1.208	0.680	1.264	1.304	0.973	0.407	0.454	6.196	3.652	1.172	
0.75	1.1	44.169	55.788	9.268	319.270	1.193	7.887	1228.021	1.095	0.613	1.188	1.209	0.829	0.478	0.502	3.978	1.534	0.531	
0.75	1.15	44.409	77.064	10.670	969.644	1.169	8.973	1504.169	1.143	0.662	1.244	1.263	0.922	0.435	0.489	5.177	2.053	0.698	
0.75	1.2	44.041	116.054	12.092	3088.380	1.166	10.234	1629.991	1.197	0.731	1.274	1.309	0.988	0.425	0.478	5.675	2.642	0.813	
0.8	1.1	39.297	57.230	10.230	496.682	1.235	8.185	1163.873	1.109	0.665	1.193	1.212	0.878	0.468	0.510	4.301	1.185	0.399	
0.8	1.15	39.287	79.925	10.473	1374.399	1.181	9.195	1237.723	1.161	0.721	1.234	1.260	0.896	0.496	0.507	4.974	1.764	0.545	
0.8	1.2	39.492	119.181	12.826	3798.235	1.153	10.314	2009.456	1.188	0.790	1.282	1.308	0.962	0.440	0.534	6.097	2.054	0.609	
0.85	1.1	35.004	58.494	9.878	470.637	1.222	8.327	1098.367	1.127	0.715	1.199	1.216	0.782	0.613	0.517	3.720	1.100	0.319	
0.85	1.15	35.235	83.566	11.350	1692.525	1.156	9.368	1553.895	1.163	0.776	1.259	1.269	0.843	0.554	0.559	4.236	1.786	0.507	
0.85	1.2	35.324	124.731	12.091	3358.091	1.166	10.653	2287.650	1.195	0.848	1.282	1.318	0.936	0.490	0.569	5.210	2.123	0.589	
0.9	1.1	31.372	61.506	10.939	773.097	1.201	8.938	1361.269	1.125	0.771	1.220	1.220	0.756	0.717	0.493	3.280	0.987	0.246	
0.9	1.15	31.134	86.424	11.210	885.785	1.252	9.820	1864.311	1.154	0.838	1.270	1.270	0.836	0.617	0.560	3.535	1.818	0.381	
0.9	1.2	31.579	126.927	12.613	3144.213	1.217	10.945	2054.908	1.209	0.916	1.302	1.323	0.846	0.612	0.599	4.085	1.731	0.417	
0.95	1.1	27.877	63.855	11.437	2962.060	1.103	9.254	1144.728	1.163	0.829	1.226	1.226	0.713	0.734	0.569	3.206	0.920	0.167	
0.95	1.15	31.135	88.035	11.775	3054.531	1.155	9.950	1165.923	1.212	0.903	1.262	1.276	0.781	0.724	0.565	2.911	1.221	0.238	
0.95	1.2	28.166	131.369	13.791	854.627	1.294	11.285	2306.283	1.218	0.979	1.312	1.324	0.872	0.615	0.617	4.394	2.626	0.490	
1	1.1	24.681	66.239	11.959	6072.826	0.967	9.691	1512.814	1.165	0.882	1.210	1.227	0.672	0.851	0.552	2.350	1.002	0.136	
1	1.15	24.957	91.897	12.753	1658.527	1.200	10.396	913.077	1.256	0.962	1.248	1.280	0.832	0.657	0.634	2.488	1.711	0.225	
1	1.2	24.999	133.209	13.322	773.319	1.332	11.525	916.374	1.304	1.047	1.325	1.318	0.840	0.632	0.684	3.943	4.269	0.452	
1.05	1.1	21.875	70.602	12.960	2830.360	1.152	10.302	2751.701	1.152	0.943	1.231	1.241	0.671	0.888	0.571	1.748	2.309	0.199	
1.05	1.15	21.990	98.120	13.257	2803.448	1.193	11.314	1549.808	1.248	1.022	1.238	1.290	0.749	0.811	0.617	2.033	3.290	0.281	
1.05	1.2	22.009	130.896	23.068	2403.125	1.317	12.535	803.453	1.317	1.063	1.279	1.325	0.804	0.729	0.656	5.116	8.890	0.786	